Presynaptic NMDA receptors facilitate short-term plasticity and BDNF release at hippocampal mossy fiber synapses

Pablo J. Lituma[1], Hyung-Bae Kwon[1,4], Karina Alviña[1,5], Rafael Lujan[3], Pablo E. Castillo[1,2]*

[1] Dominick P. Purpura Department of Neuroscience, Albert Einstein College of Medicine, Bronx, NY 10461, U.S.A.
[2] Department of Psychiatry and Behavioral Sciences, Albert Einstein College of Medicine, Bronx, NY 10461, U.S.A.
[3] Instituto de Investigación en Discapacidades Neurológicas (IDINE), Facultad de Medicina, Universidad Castilla-La Mancha, 02008 Albacete, Spain.
[4] Present address: The Solomon H. Snyder Department of Neuroscience, John Hopkins University, School of Medicine, Baltimore, MD 21205, U.S.A.
[5] Present address: Department of Neuroscience, University of Florida, 1149 Newell Drive, Room L1-100, Gainesville, FL, 32611, U.S.A.

Running title: Role of presynaptic NMDA receptors in short-term plasticity

Keywords: CA3, ionotropic, hippocampus, presynaptic calcium, autoreceptors

* To whom correspondence should be addressed:

Pablo E. Castillo, MD/PhD
Dominick P. Purpura Department of Neuroscience
Albert Einstein College of Medicine
1410 Pelham Parkway South
Kennedy Center, Room 703
Bronx, NY 10461, USA
Email: pablo.castillo@einsteinmed.org

Author Contributions: PJL and PEC designed the experiments. Except for the electron microscopy experiments, PJL performed all experiments included in this study and analyzed data. HBK performed preliminary experiments and made observations that triggered this study. RL performed electron microscopy experiments and analyzed the data. KA set up the 2P system in the Castillo Lab and validated acquisition and analysis methods. PJL and PEC wrote the first manuscript which was edited by all authors.

Funding sources: This work supported by the NIH (F31-MH109267 to PJL; R01 MH116673, R01MH125772, and R01 NS 113600 to P.E.C.) and by the Spanish Ministerio de Economia y Competitividad (RTI2018-095812-B-I00) and Junta de Comunidades de Castillo-La Mancha (SBPLY/17/180501/000229) to RL.

Acknowledgements: We thank all the Castillo lab members for invaluable discussions. We also thank Dr. Hyungju Park for his generous gift of the BDNF-phluorin DNA construct, Dr. Michael Higley for sharing *Grin1* floxed mice, and Dr. Pascal Kaeser for his generous gift of the Cre-dependent ChIEF DNA construct.

Title: 112 characters (with spaces)
Summary: 138 words, 1080 characters with spaces
Main text (excluding Summary, Methods, references and figure legends): 4,490
Figures: 8
Supplementary figures: 12

Summary

Neurotransmitter release is a highly controlled process by which synapses can critically regulate information transfer within neural circuits. While presynaptic receptors –typically activated by neurotransmitters and modulated by neuromodulators– provide a powerful way of fine-tuning synaptic function, their contribution to activity-dependent changes in transmitter release remains poorly understood. Here, we report that presynaptic NMDA receptors (preNMDARs) at hippocampal mossy fiber boutons can be activated by physiologically relevant patterns of activity and selectively enhance short-term synaptic plasticity at mossy fiber inputs onto CA3 pyramidal cells and mossy cells, but not onto inhibitory interneurons. Moreover, preNMDARs facilitate brain-derived neurotrophic factor (BDNF) release and contribute to presynaptic calcium rise. Taken together, our results indicate that by increasing presynaptic calcium, preNMDARs fine tune mossy fiber neurotransmission and can control information transfer during dentate granule cell burst activity that normally occur *in vivo*.

Introduction

Neurotransmission is a dynamic and highly regulated process. The activation of ionotropic and metabotropic presynaptic autoreceptors provides a powerful way of fine-tuning neurotransmission via the facilitation or inhibition of neurotransmitter release (Burke & Bender, 2019; Engelman & MacDermott, 2004; Miller, 1998; Pinheiro & Mulle, 2008; Schicker et al., 2008). Due to their unique functional properties, including high calcium-permeability, slow kinetics and well-characterized role as coincidence-detectors (Cull-Candy et al., 2001; Lau & Zukin, 2007; Paoletti et al., 2013; Traynelis et al., 2010), presynaptic NMDA receptors (preNMDARs) have received particular attention (Banerjee et al., 2016; Bouvier et al., 2015; Bouvier et al., 2018; Duguid, 2013; Duguid & Smart, 2009; Wong et al., 2020). Regulation of neurotransmitter release by NMDA autoreceptors in the brain was suggested three decades ago (Martin et al., 1991). Anatomical evidence for preNMDARs arose from an immuno-electron microscopy study revealing NMDARs at the mossy fiber giant bouton of the monkey hippocampus (Siegel et al., 1994), followed by functional studies in the entorhinal cortex indicating that preNMDARs tonically increase spontaneous glutamate release and also facilitate evoked release in a frequency-dependent manner (Berretta & Jones, 1996; Woodhall et al., 2001). Since these early studies, although evidence for preNMDARs has accumulated throughout the brain (Banerjee et al., 2016; Bouvier et al., 2018; Duguid & Smart, 2009), the presence and functional relevance of preNMDARs at key synapses in the brain have been called into question (Carter & Jahr, 2016; Duguid, 2013).

Mossy fibers (mf) – the axons of dentate granule cells (GCs) – establish excitatory synapses onto proximal dendrites of CA3 pyramidal neurons, thereby conveying a major excitatory input to the hippocampus proper (Amaral et al., 2007; Henze et al., 2000). This synapse displays uniquely robust frequency facilitation both *in vitro* (Nicoll & Schmitz, 2005; Salin et al., 1996; Vyleta et al.,

2016) and *in vivo* (Hagena & Manahan-Vaughan, 2010; Vandael et al., 2020). The molecular basis of this short-term plasticity is not fully understood but likely relies on diverse presynaptic mechanisms that increase glutamate release (Jackman & Regehr, 2017; Rebola et al., 2017). Short-term, use-dependent facilitation is believed to play a critical role in information transfer, circuit dynamics and short-term memory (Abbott & Regehr, 2004; Jackman & Regehr, 2017; Klug et al., 2012). The mf-CA3 synapse can strongly drive the CA3 network during short bursts of presynaptic activity (Chamberland et al., 2018; Henze et al., 2002; Vyleta et al., 2016; Zucca et al., 2017), an effect that likely results from two key properties of this synapse, namely, its strong frequency facilitation and proximal dendritic localization. In addition to CA3 pyramidal neurons, mf axons establish synaptic connections with hilar mossy cells (MC) and inhibitory interneurons (IN) (Amaral et al., 2007; Henze et al., 2000). These connections also display robust short-term plasticity (Lysetskiy et al., 2005; Toth et al., 2000), which may contribute significantly to information transfer and dynamic modulation of the dentate gyrus (DG)-CA3 circuit (Bischofberger et al., 2006; Evstratova & Toth, 2014; Lawrence & McBain, 2003). Despite early evidence for preNMDARs at mf boutons (Siegel et al., 1994), whether these receptors modulate neurotransmission at mf synapses is unknown. Intriguingly, mfs contain one of the highest expression levels of brain-derived neurotrophic factor, BDNF (Conner et al., 1997). While preNMDARs were implicated in BDNF release at corticostriatal synapses (Park et al., 2014), whether putative preNMDARs impact BDNF release at mf synapses remains unexplored.

Here, to examine the potential presence and impact of preNMDARs at mf synapses, we utilized multiple approaches, including immunoelectron microscopy, selective pharmacology for NMDARs, a genetic knockout strategy to remove NMDARs from presynaptic GCs, two-photon imaging of BDNF release, and presynaptic Ca^{2+} signals in acute rodent hippocampal slices. Our findings indicate that preNMDARs contribute to mf short-term plasticity and promotes BDNF release likely by increasing presynaptic Ca^{2+}. Thus, preNMDARs at mfs may facilitate information

129 transfer and provide an important point of regulation in the DG – CA3 circuit by regulating both
130 glutamate and BDNF release.
131
132 **Results**
133
134 **Electron microscopy reveals presynaptic NMDA receptors at mossy fiber terminals**
135 To determine the potential localization of NMDA receptors at the mf terminals of the rodent
136 hippocampus, we performed electron microscopy and post-embedding immunogold labeling in
137 rats using a validated antibody for the obligatory subunit GluN1 (Petralia et al., 1994; Siegel et
138 al., 1994; Takumi et al., 1999; Watanabe et al., 1998). Gold particles were detected in the main
139 body of the postsynaptic density as well as presynaptic mf terminals (**Figure 1A-C**). GluN1
140 localized in mf boutons in a relatively high proportion to the active zone, as compared to
141 associational-commissural (ac) synapse in the same CA3 pyramidal neuron (**Figure 1D**; mf,
142 ~32% presynaptic particles; ac, <10% presynaptic particles; n = 3 animals). Similar quantification
143 for AMPA receptors did not reveal presynaptic localization of these receptors in either mf or
144 associational commissural synapses (**Figure S1A-C**; ~5% presynaptic particles, n = 3 animals).
145 Together, these results provide anatomical evidence for preNMDARs at mf-CA3 synapses.
146
147 **Both NMDAR antagonism and genetic deletion from presynaptic granule cells reduce**
148 **mossy fiber low-frequency facilitation**
149 Presynaptic short-term plasticity, in the form of low-frequency (~1 Hz) facilitation (LFF), is uniquely
150 robust at the mf-CA3 synapse (Nicoll & Schmitz, 2005; Salin et al., 1996). To test a potential
151 involvement of preNMDARs in LFF, we monitored AMPAR-mediated excitatory postsynaptic
152 currents (EPSCs) from CA3 pyramidal neurons in acute rat hippocampal slices. Neurons were
153 held at V_h= -70 mV to minimize postsynaptic NMDAR conductance, and mfs were focally
154 stimulated with a bipolar electrode (theta glass pipette) placed in *stratum lucidum* ~100 μm from

155 the recorded cell. LFF was induced by stepping the stimulation frequency from 0.1 Hz to 1 Hz for
156 ~2 min in the presence of picrotoxin (100 μM) to block fast inhibitory synaptic transmission, and
157 a low concentration of the AMPAR noncompetitive antagonist LY303070 (0.5 μM) to minimize
158 CA3-CA3 recurrent activity (Kwon & Castillo, 2008). Bath-application of the NMDAR irreversible
159 open channel blocker MK-801 (50 μM) significantly reduced LFF (**Figure 1E**). In addition, the
160 competitive NMDAR antagonists D-APV (100 μM) or R-CPP (50 μM) yielded a comparable
161 reduction of facilitation (**Figure 1F**). To confirm that these synaptic responses were mediated by
162 mfs, the mGluR2/3 agonist DCG-IV (1 μM) was applied at the end of all recordings (Kamiya et al.,
163 1996). To control for stability, we performed interleaved experiments in the absence of NMDAR
164 antagonists and found that LFF remained unchanged (**Figure S2A**). These findings indicate
165 NMDAR antagonism reduces mf-CA3 short-term plasticity (LFF), suggesting that preNMDARs
166 could contribute to this form of presynaptic plasticity.
167
168 The reduction in facilitation of AMPAR-transmission could be due to dampening of CA3 recurrent
169 activity by NMDAR antagonism (Henze et al., 2000; Kwon & Castillo, 2008; Nicoll & Schmitz,
170 2005). To discard this possibility, we repeated our experiments in a much less excitable network
171 in which AMPAR-mediated synaptic transmission was selectively blocked by a high concentration
172 of the noncompetitive antagonist LY303070 (15 μM) and monitored the kainate receptor (KAR)-
173 mediated component of mf synaptic transmission (Castillo et al., 1997; Kwon & Castillo, 2008).
174 In addition, 2 mM MK-801 was included in the intracellular recording solution to block postsynaptic
175 NMDARs (Corlew et al., 2008). To further ensure postsynaptic NMDAR blockade, we voltage-
176 clamped the CA3 pyramidal neuron at -70 mV and waited until NMDAR-mediated transmission
177 was eliminated and only KAR-EPSCs remained. Under these recording conditions, bath-
178 application of MK-801 (50 μM) also reduced LFF of KAR-mediated transmission (**Figure 1G**),
179 whereas LFF remained unchanged in interleaved control experiments (**Figure S2B**). At the end
180 of these recordings**,** 10 μM NBQX was applied to confirm KAR-transmission (**Figure 1G; Figure**

181 **S2B**) (Castillo et al., 1997; Kwon & Castillo, 2008). It is therefore unlikely that the reduction of LFF
182 mediated by NMDAR antagonism could be explained by recurrent network activity, suggesting a
183 direct effect on transmitter release.
184
185 To further support a role of preNMDARs in mf LFF, we took a genetic approach by conditionally
186 removing NMDARs from GCs in *Grin1* floxed mice. To this end, an AAV5-CamKII-Cre-GFP virus
187 was bilaterally injected in the DG to selectively delete *Grin1* expression, whereas AAV5-CamKII-
188 eGFP was injected in littermates as a control at postnatal days 16-20 in both groups (**Figure 2A**).
189 Two weeks after surgery, we prepared acute hippocampal slices and examined the efficacy of
190 *Grin1* deletion by analyzing NMDAR-mediated transmission in GFP^+ GCs of *Grin1*-cKO and
191 control mice. We confirmed that in contrast to control mice, no NMDAR-EPSCs were elicited by
192 electrically stimulating medial perforant path inputs in *Grin1*-cKO GCs voltage-clamped at +40
193 mV in the presence of 100 μM picrotoxin and 10 μM NBQX (**Figure 2B**). As expected, the
194 NMDAR/AMPAR ratio was significantly reduced in *Grin1*-cKO mice compared to control (**Figure**
195 **2C**). Only acute slices that exhibited robust GFP fluorescence in the DG were tested for LFF of
196 AMPAR-transmission in CA3. We found that LFF was significantly reduced in *Grin1*-cKOs as
197 compared to controls (**Figure 2D**), indicating that genetic removal of NMDARs from GCs
198 recapitulated NMDAR antagonism (**Figure 1E-G**). *Grin1* deletion did not affect basal transmitter
199 release as indicated by a comparable paired-pulse ratio to control (Control: 2.5 ± 0.36, n = 13
200 cells; *Grin1* cKO: 2.4 ± 0.31, n = 13 cells; U > 0.5, Mann-Whitney test). Collectively, our findings
201 using two distinct approaches strongly suggest that NMDAR activation in GCs increases LFF of
202 mf-CA3 synaptic transmission.
203
204 **Reduced facilitation by NMDAR antagonism is independent of the granule cell**
205 **somatodendritic compartment**
206 Bath application of MK-801 could have blocked dendritic NMDARs in GCs and potentially affected

207 transmitter release (Christie & Jahr, 2008; Duguid, 2013). To address this possibility, we repeated
208 our experiments after performing a surgical cut in the granular layer of the DG in order to isolate
209 mf axons from GCs (**Figure S3A**). Under these conditions, MK-801 bath application still reduced
210 LFF (**Figure 3A**), and LFF was stable in control, acutely transected axons (**Figure 3B**). In addition,
211 puffing D-APV (2 mM) in *stratum lucidum* near (~200 μm) the recorded neuron also reduced LFF
212 (**Figure 3C**), whereas puffing ACSF had no effect (**Figure 3D**). Lastly, in a set of control
213 experiments, we confirmed that D-APV puffs were sufficient to transiently block NMDAR-mediated
214 transmission in CA3 but not in DG (**Figure S3B,C**). Together, these results support the notion that
215 LFF reduction was due to the blockade of preNMDARs but not somatodendritic NMDARs on GCs.
216

217 **PreNMDARs boost information transfer by enhancing burst-induced facilitation at mossy**
218 **fiber synapses**

219 GCs *in vivo* typically fire in brief bursts (Diamantaki et al., 2016; GoodSmith et al., 2017; Henze
220 et al., 2002; Pernia-Andrade & Jonas, 2014; Senzai & Buzsaki, 2017). To test whether
221 preNMDARs contribute to synaptic facilitation that occurs during more physiological patterns of
222 activity, mfs were activated with brief bursts (5 stimuli, 25 Hz). We first took an optogenetic
223 approach and used a Cre-dependent ChIEF virus to selectively light-activate mf-CA3 synapses
224 in *Grin1*-cKO and control mice. Thus, animals were injected with a mix of AAV5-CamKII-CreGFP
225 + AAV-DJ-FLEX-ChIEF-tdTomato viruses in the DG (**Figure 4A**). At least four weeks after surgery,
226 acute slices were prepared and burst-induced facilitation of AMPAR-mediated transmission in
227 CA3 was assessed (**Figure 4B,C**). Burst-induced facilitation triggered by light stimulation and
228 measured as the ratio of EPSCs elicited by the 5th and 1st pulse (P5/P1 ratio), was significantly
229 reduced in *Grin1*-cKO animals as compared to controls. Because these bursts of activity can
230 activate the CA3 network (Henze et al., 2000; Kwon & Castillo, 2008; Nicoll & Schmitz, 2005), we
231 next monitored KAR-EPSCs under conditions of low excitability (as in Figure 1G). MK-801 bath
232 application also reduced burst-induced facilitation, whereas facilitation remained unchanged in

233 naïve slices (**Figure 4D,E**). In a separate set of experiments, we confirmed the reduction of MK-
234 801 on burst-induced facilitation under more physiological recording conditions (**Figure S5**).
235 Lastly, we tested whether preNMDARs, by facilitating glutamate release during bursting activity,
236 could bring CA3 pyramidal neurons to threshold and trigger postsynaptic action potentials. To test
237 this possibility, we monitored action potentials elicited by KAR-EPSPs (resting membrane
238 potential -70 ± 2 mV) from CA3 pyramidal neurons intracellularly loaded with 2 mM MK-801. Under
239 these recording conditions, MK-801 bath application significantly reduced the mean number of
240 spikes per burst (**Figure 4F**). No changes in mean spikes per burst were observed in naïve slices
241 over time (**Figure 4G**). Application of 10 μM NBQX at the end of these experiments confirmed
242 that action potentials were induced by KAR-mediated synaptic responses. Consistent with these
243 observations, MK-801 also reduced the mean number of spikes per burst when AMPAR-mediated
244 action potentials were recorded from CA3 pyramidal neurons (**Figure S6**). In control experiments,
245 we found that intracellular MK-801 effectively blocked postsynaptic NMDAR transmission during
246 burst stimulation (**Figure S4B**). Altogether, these results indicate that preNMDARs at mf-CA3
247 synapses can contribute to information transfer from the DG to CA3.
248
249
250 **PreNMDARs contribute to presynaptic calcium rise and can be activated by glutamate**
251 PreNMDARs could facilitate glutamate and BDNF release by increasing presynaptic Ca^{2+} rise
252 (Bouvier et al., 2016; Buchanan et al., 2012; Corlew et al., 2008; Park et al., 2014). To test this
253 possibility at mf-CA3 synapses, we combined a conditional knockout strategy with Ca^{2+} imaging
254 using two-photon laser scanning microscopy. We first deleted preNMDARs by injecting AAV5-
255 CamKII-mCherry-Cre virus in the DG of *Grin1* floxed mice, and littermate animals injected with
256 AAV5-CamKII-mCherry virus served as control (**Figure 5A**). Two weeks after surgery, we
257 confirmed the efficacy of *Grin1* deletion by activating medial perforant path inputs and monitoring
258 NMDAR/AMPAR ratios in GCs of control and *Grin1*-cKO animals (**Figure 5A**). Virtually no

259 NMDAR-EPSCs were detected at V_h= +40 mV in *Grin1*-cKO animals (**Figure 5A**). Acute slices
260 that exhibited robust mCherry fluorescence in the DG were used for Ca^{2+} imaging experiments.
261 To maximize our ability to detect preNMDAR-mediated Ca^{2+} signals, we used a recording solution
262 that contained 0 mM Mg^{2+}, 4 mM Ca^{2+} and 10 μM D-Serine (Carter & Jahr, 2016). GCs expressing
263 mCherry were patch-loaded with 35 μM Alexa 594 (used as morphological dye) and 200 μM Fluo-
264 5F, and mf axons were imaged and followed towards CA3 until giant boutons (white arrows) were
265 identified (**Figure 5B**). We found that Ca^{2+} transients (CaTs) elicited by direct current injection in
266 the GC soma (5 action potentials, 25 Hz) were significantly smaller in *Grin1*-cKO animals as
267 compared to control (**Figure 5C-E**). In addition, NMDAR antagonism with D-APV reduced
268 presynaptic Ca^{2+} rise even under more physiological Mg^{+2} concentration in acute rat hippocampal
269 slices (**Figure S7**). Thus, preNMDARs contribute significantly to presynaptic Ca^{2+} rise in mf
270 boutons, and by this means likely facilitates synaptic transmission, although a potential
271 contribution of Ca^{2+} rise-independent effects cannot be discarded.
272
273 Lastly, we sought to determine if direct activation of preNMDARs could drive Ca^{2+} influx in mf giant
274 boutons. To test this possibility, we elicited CaTs by two-photon glutamate uncaging (2PU) on mf
275 boutons of control and *Grin1*-cKO animals (**Figure 6A**). As previously described, mCherry GCs
276 were patch-loaded with Alexa 594 and Fluo-5F in a recording solution designed to maximize the
277 detection of preNMDAR-mediated Ca^{2+} signals (as in Figure 5). We first confirmed that glutamate
278 2PU-induced CaTs in dendritic spine heads of GCs were strongly reduced in *Grin1*-cKO animals
279 as compared to controls (**Figure 6B,C**). To verify that reduced Ca^{2+} signals (ΔG/R) were a result
280 of *Grin1* deletion and not differences in uncaging laser power, we performed a laser power
281 intensity–response curve, and found that *Grin1*-cKO animals exhibited reduced ΔG/R signals as
282 compared to control regardless of laser power intensity (**Figure S8**). We next measured
283 glutamate 2PU-induced CaTs in mf giant boutons (identified as in Figure 5B) and found that single
284 uncaging pulses were insufficient to drive detectable CaTs in control boutons (**Figure S9**).

285 However, a burst of 2PU stimulation (5 pulses, 25 Hz) induced CaTs in mf boutons of control but
286 not in *Grin1*-cKO animals (**Figure 6D,E**). Additionally, CaTs elicited by 2PU stimulation were
287 abolished by D-APV application (**Figure S10**). These findings indicate that brief bursts of
288 glutamate 2PU, a manipulation that mimics endogenous release of glutamate during physiological
289 patterns of activity, induces presynaptic Ca^{2+} influx in mf boutons by activating preNMDARs.
290

291 **PreNMDARs promote BDNF release from mossy fiber boutons**

292 Previous work implicated preNMDARs in the release of BDNF at corticostriatal synapses following
293 burst stimulation and presynaptic Ca^{2+} elevations (Park et al., 2014). Given the high expression
294 levels of BDNF in mfs (Conner et al., 1997; Yan et al., 1997), we examined the potential role for
295 preNMDARs in BDNF release from mf terminals. To this end, a Cre-dependent BDNF reporter
296 (BDNF-pHluorin) was injected in *Grin1*-floxed and control animals. Littermate mice were injected
297 with a mix of AAV5-CamKII-mCherry-Cre + AAV-DJ-DIO-BDNF-pHluorin viruses in the DG
298 (**Figure 7A**). At least four weeks after surgery, acute slices were prepared for two-photon laser
299 microscopy to image mf boutons. After acquiring a stable baseline of BDNF-pHluorin signals, mfs
300 were repetitively activated (see Methods) (**Figure 7B**). BDNF-pHluorin signals were analyzed by
301 measuring ΔF/F, where ΔF/F reductions indicate BDNF release (Park et al., 2014). We found that
302 GluN1-deficient mf boutons showed a significant (~50%) impairment in BDNF release as
303 compared to control (**Figure 7C-D**). Furthermore, using a more physiological pattern of burst
304 stimulation, GluN1-lacking mf boutons still displayed altered BDNF release as compared to
305 control (**Figure S11**). Taken together, our results suggest preNMDARs contribute significantly to
306 BDNF release during repetitive or burst stimulation of mf synapses.
307

308 **PreNMDAR-mediated regulation of mossy fiber synapses is input-specific**

309 In addition to providing a major excitatory input to the hippocampus proper, mf axons also synapse
310 onto excitatory hilar mossy cells and inhibitory neurons in CA3 (Amaral et al., 2007; Henze et al.,

311 2000; Lawrence & McBain, 2003). To test whether preNMDARs could also play a role at these
312 synapses, we visually patched mossy cells and interneurons in acute rat hippocampal slices,
313 loaded them with 35 μM Alexa 594 (**Figure 8A**) and 2 mM MK-801, and monitored AMPAR-
314 EPSCs (V_h = -70 mV). Unlike mf-CA3 synapses, mf synapses onto CA3 interneurons in *stratum*
315 *lucidum* do not express LFF, but can undergo burst-induced facilitation or depression (Toth et al.,
316 2000). We found that MK-801 bath application had no effect on burst-induced facilitation or
317 depression (**Figure 8B**), suggesting preNMDARs do not play a role at mf-Interneuron synapses
318 in CA3. Mf inputs onto hilar mossy cells undergo robust activity-dependent facilitation (Lysetskiy
319 et al., 2005). Similar to mf-CA3 synapses, we found that MK-801 reduced LFF (**Figure 8C**).
320 Stability experiments of mf transmission at CA3 interneurons or hilar mossy cells showed no
321 significant differences (**Figure S12**). Taken together, our findings demonstrate that preNMDARs
322 facilitate mf transmission onto excitatory neurons but not onto inhibitory interneurons.
323
324
325 **Discussion**
326
327 In this study, we provide evidence that hippocampal mf boutons express preNMDARs whose
328 activation fine-tunes mf synaptic function. Specifically, our results show that preNMDARs enhance
329 mf short-term plasticity in a target cell-specific manner. By enhancing glutamate release onto
330 excitatory but not inhibitory interneurons, preNMDARs increase GC-CA3 spike transfer.
331 Moreover, using two-photon Ca^{2+} imaging, we demonstrate that preNMDARs contribute to
332 presynaptic Ca^{2+} rise in mf boutons. Lastly, upon repetitive activity, preNMDARs promote BDNF
333 release from mf boutons. Taken together, our findings indicate that preNMDARs act as
334 autoreceptors to boost both glutamate and BDNF release at mf synapses. By regulating
335 information flow in the DG-CA3 circuit, preNMDARs may play a significant role in learning and
336 memory.

337

338 Early studies using immunoperoxidase electron microscopy revealed NMDARs in presynaptic
339 compartments in multiple brain areas (for a review, see Corlew et al., 2008). Subsequent studies
340 that used immunogold electron microscopy, a more precise localization method, identified
341 NMDARs on the presynaptic membrane in a number of brain structures, including neocortex
342 (Fujisawa & Aoki, 2003; Larsen et al., 2011), hippocampus (Berg et al., 2013; Jourdain et al.,
343 2007; McGuinness et al., 2010), and amygdala (Pickel et al., 2006). In agreement with these
344 studies, and using a previously validated antibody (Siegel et al., 1994), we identified prominent
345 presynaptic labeling of the obligatory subunit GluN1 in mf boutons (Figure 1A-D). Moreover, we
346 found that these receptors are close to the active zone and therefore well positioned to modulate
347 neurotransmitter release.

348

349 Previous work in the cerebellum and neocortex suggested that somatodendritic potentials
350 generated by NMDARs could signal to nerve terminals and lead to presynaptic Ca^{2+} elevations
351 (Christie & Jahr, 2008, 2009). Thus, changes in neurotransmitter release resulting from NMDAR
352 antagonism could be due to somatodendritic NMDARs but not necessarily preNMDARs residing
353 on nerve terminals (Duguid, 2013). However, we showed that focal NMDAR antagonism far from
354 the somatodendritic compartment and in transected axons still reduced short-term plasticity at mf
355 synapses (Figure 3), making it extremely unlikely that somatodendritic NMDARs could explain
356 our results. In further support of functional preNMDARs at mf boutons, we found that 2PU of
357 glutamate induced Ca^{2+} rise in control but not in GluN1-deficient boutons. Together, our findings
358 strongly support the presence of functional preNMDARs facilitating neurotransmission at mf-CA3
359 synapses.

360

361 There is evidence that preNMDARs can operate as coincidence detectors at some synapses
362 (Duguid, 2013; Wong et al., 2020). At the mf-CA3 synapse, we found that preNMDARs contribute

363 to LFF (i.e. 1s inter-stimulus interval). This observation is intriguing given that the presynaptic AP-
364 mediated depolarization is likely absent by the time glutamate binds to preNMDARs. However,
365 coincidence detection may not be an essential requirement for mf preNMDARs to modulate
366 glutamate release. Of note, at resting membrane potential the NMDAR conductance is not zero
367 and the driving force for Ca^{2+} influx is high (Paoletti et al., 2013; Traynelis et al., 2010). It is also
368 conceivable that mf preNMDARs exhibit low-voltage dependence, as it has been reported at other
369 synapses (Wong et al., 2020). Remarkably, the somatodendritic compartment of GCs can
370 generate sub-threshold depolarizations at mf terminals (a.k.a. excitatory presynaptic potentials)
371 (Alle & Geiger, 2006). By alleviating the magnesium blockade, these potentials might reduce the
372 need for coincidence detection and transiently boost the functional impact of mf preNMDARs.
373
374 While the presence of preNMDARs is downregulated during development both in neocortex
375 (Corlew et al., 2007; Larsen et al., 2011) and hippocampus (Mameli et al., 2005), we were able to
376 detect functional preNMDARs in young adult rats (P17-P28) and mice (P30-P44), once mf
377 connections are fully developed (Amaral & Dent, 1981). Functional preNMDARs have been
378 identified in axonal growth cones of hippocampal and neocortical neurons, suggesting these
379 receptors are important for regulating early synapse formation (Gill et al., 2015; Wang et al., 2011).
380 Because GCs undergo adult neurogenesis, and adult born GCs establish new connections in the
381 mature brain, preNMDARs could also play an important role at immature mf synapses and
382 functional integration of new born GCs into the mature hippocampus (Toni & Schinder, 2015).
383 Moreover, experience can modulate the expression and composition of preNMDARs in neocortex
384 (Larsen et al., 2014), a possibility not investigated in our study.
385
386 The glutamate that activates preNMDARs may originate from the presynaptic terminal, the
387 postsynaptic cell, nearby synapses or neighboring glial cells. Our results indicate that activation
388 of preNMDARs at mf synapses requires activity-dependent release of glutamate that likely arises

389 from mf boutons, although other sources cannot be discarded, including astrocytes. For instance,
390 at medial entorhinal inputs to GCs, preNMDARs appear to be localized away from the presynaptic
391 release sites and facing astrocytes, consistent with preNMDAR activation by gliotransmitters
392 (Jourdain et al., 2007; Savtchouk et al., 2019). In contrast, at mf-CA3 synapses we found that
393 preNMDARs are adjacent to the release sites suggesting a direct control on glutamate release
394 from mf boutons.
395
396 The precise mechanism by which preNMDARs facilitate neurotransmitter release is poorly
397 understood but it may include Ca^{2+} influx through the receptor and depolarization of the
398 presynaptic terminal with subsequent activation of voltage-gated Ca^{2+} channels (Banerjee et al.,
399 2016; Corlew et al., 2008). In support of this mechanism is the high Ca^{2+} permeability of NMDARs
400 (Paoletti et al., 2013; Rogers & Dani, 1995). Besides, presynaptic subthreshold depolarization
401 and subsequent activation of presynaptic voltage-gated Ca^{2+} channels is a common mechanism
402 by which presynaptic ionotropic receptors facilitate neurotransmitter release (Engelman &
403 MacDermott, 2004; Pinheiro & Mulle, 2008). PreNMDARs may also act in a metabotropic manner
404 (Dore et al., 2016) and facilitate spontaneous transmitter release independent of Ca^{2+}-influx
405 (Abrahamsson et al., 2017). Our findings demonstrating that the open channel blocker MK-801
406 robustly reduced short-term plasticity at mf synapses support an ionotropic mechanism that
407 involves Ca^{2+} influx through preNMDARs. A previous study failed to observe Ca^{+2} reductions in
408 mf boutons by DL-APV (Liang et al., 2002). A combination of factors could account for this
409 discrepancy with our study, including a stronger mf repetitive stimulation (20 pulses, 100 Hz)
410 which may overcome a less potent NMDAR antagonism and/or the need for preNMDAR activity,
411 as well as the use of a higher affinity Ca^{2+} indicator (Fura-2 AM) and a lower spatiotemporal
412 resolution imaging approach. Nevertheless, in line with previous studies that detected presynaptic
413 Ca^{2+} rises following local activation of NMDARs (e.g. NMDA or glutamate uncaging) in visual
414 cortex (Buchanan et al., 2012) and cerebellum (Rossi et al., 2012), we provide direct evidence

415 that preNMDAR activation either by repetitive activation of mfs or 2PU of glutamate increases
416 presynaptic Ca^{2+} (Figures 5 and 6). Although the Ca^{2+} targets remain unidentified, these may
417 include proteins of the release machinery, calcium-dependent protein kinases and phosphatases,
418 and Ca^{2+} release from internal stores (Banerjee et al., 2016). In addition to facilitating evoked
419 neurotransmitter release, preNMDARs can promote spontaneous neurotransmitter release as
420 indicated by changes in miniature, action potential-independent activity (e.g. mEPSCs) (for recent
421 reviews, see Banerjee et al., 2016; Kunz et al., 2013; Wong et al., 2020). A potential role for
422 preNMDARs in spontaneous, action potential-independent release at mf synapses cannot be
423 discarded.
424
425 Our results show that activation of preNMDARs by physiologically relevant patterns of presynaptic
426 activity enhanced mf transmission and DG-CA3 information transfer (Figure 4). A previous study
427 reported NMDAR genetic deletion in GCs resulted in memory deficits (e.g. pattern separation)
428 (McHugh et al., 2007). Although the mechanism is unclear, it could involve activity-dependent
429 preNMDAR regulation of mf excitatory connections. We also found that preNMDARs facilitate
430 neurotransmitter release in a target cell-specific manner. Like in neocortex (Larsen & Sjostrom,
431 2015), such specificity strongly suggests that preNMDARs have distinct roles in controlling
432 information flow in cortical microcircuits. Thus, preNMDAR facilitation of mf synapses onto
433 glutamatergic neurons but not GABAergic interneurons (Figure 8) may fine-tune the CA3 circuit
434 by increasing the excitatory/inhibitory balance.
435
436 Given the multiple signaling cascades known to regulate NMDARs (Lau & Zukin, 2007; Sanz-
437 Clemente et al., 2013), preNMDARs at mf synapses may provide an important site of
438 neuromodulatory control. PreNMDARs have been implicated in the induction of LTP and LTD at
439 excitatory or inhibitory synapses in several brain areas (Banerjee et al., 2016; Wong et al., 2020).
440 While most evidence, at least using robust induction protocols *in vitro,* indicates that long-term

441 forms of presynaptic plasticity at mf synapses can occur in the absence of NMDAR activation
442 (Castillo, 2012; Nicoll & Schmitz, 2005), our findings do not discard the possibility that
443 preNMDARs could play a role *in vivo* during subtle presynaptic activities. As previously reported
444 for corticostriatal LTP (Park et al., 2014), preNMDARs could regulate long-term synaptic plasticity
445 by controlling BDNF release, which is consistent with BDNF-TrkB signaling being implicated in
446 mf-CA3 LTP (Schildt et al., 2013). In addition, BDNF could facilitate glutamate release by
447 enhancing NMDAR function at the presynapse, as previously suggested (W. Chen et al., 2014;
448 Madara & Levine, 2008), although the precise mechanism(s) remain unclear. By potentiating mf-
449 CA3 transmission, BDNF could also promote epileptic activity (McNamara & Scharfman, 2012).
450 Lastly, dysregulation of NMDARs is commonly implicated in the pathophysiology of brain
451 disorders such as schizophrenia, autism, and epilepsy (Lau & Zukin, 2007; Paoletti et al., 2013).
452 PreNMDAR expression and function have been suggested to be altered in experimental models
453 of disease, including neuropathic pain (Y. Chen et al., 2019; Zeng et al., 2006), and epilepsy (Yang
454 et al., 2006). At present, however, *in vivo* evidence for the involvement of preNMDARs in brain
455 function and disease is rather indirect (Bouvier et al., 2015; Wong et al., 2020). The development
456 of specific preNMDAR tools is required to determine the functional impact of these receptors *in*
457 *vivo*.
458
459
460 **Methods**
461

Key Resources Table				
Reagent type (species) or resource	**Designation**	**Source or reference**	**Identifiers**	**Additional information**

strain, strain background (*rattus norvegicus* male and female)	Rat: Sprague-Dawley	Charles River	Strain code: 400	
strain, strain background (*Mus musculus*, male and female)	Mouse: GluN1fl/fl (B6.129S4-Grin1tm2Stl/J)	Dr. Michael Higley /The Jackson Laboratory	RRID: IMSR_JAX: 005246	
strain, strain background (*Mus musculus* male and female)	Mouse: C57Bl6/J	Charles River	Strain code: 027	
antibody	(Include host species and clonality) Mouse, Monoclonal, anti-NMDAR1	Millipore	Cat# MAB363	10 µg/mL
antibody	Rabbit, Polyclonal, anti-GluA1-4, (pan-AMPA)	Dr. Elek Molnar /Bristol University	Generated by Dr. Elek Molnar	10 µg/mL
antibody	Goat anti-rabbit IgG conjugated gold particles	Nanoprobes Inc	#2003-0.5ML	1:100
recombinant DNA reagent	AAV5-CamKII-GFP-Cre	Penn Vector Core	AV-5-PV2521	Available on Addgene
recombinant DNA reagent	AAV5-CamKII-eGFP	Penn Vector Core	AV-5-PV1917	Available on Addgene

recombinant DNA reagent	AAV5-CamKII-mcherry-Cre	UNC Vector Core	See website	https://wwwmed.unc.edu/genetherapy/vectorcore/in-stock-aav-vectors/
recombinant DNA reagent	AAV5-CamKII-mcherry	UNC Vector Core-Dr. Karl Deisseroth Control Fluorophores	See website	https://wwwmed.unc.edu/genetherapy/vectorcore/in-stock-aav-vectors/
recombinant DNA reagent	AAV-DJ-flex-OChIEF-tdTomato	Dr. Pascal Kaeser PMID: **29398114**	Generated at UNC Vector Core	Custom Order
recombinant DNA reagent	AAV-DJ-DIO-BDNF-phluorin	Dr. Hyungju Park PMID: **25467984**	Generated at UNC Vector Core	Custom Order
chemical compound, drug	Ketamine	Merial	Cat#03661103001904	
chemical compound, drug	Xylazine	Calier	Cat#20100-003	
chemical compound, drug	Paraformaldehyde	Scharlau	PA0095	
chemical compound, drug	Glutaraldehyde	Electron Microscopy Sciences	Cat#16210	
chemical compound, drug	Picric Acid	Panreac	Cat#141048.1609	

chemical compound, drug	Phosphate Buffer		Scharlau	SO03321000	
chemical compound, drug	Human serum albumin		SigmaMillipore	A-1653	
chemical compound, drug	TBS	TRIZMA BASE	SigmaMillipore	T1503	
		Trizma HCl		T3253	
chemical compound, drug	Triton X-100		SigmaMillipore	T8787	
chemical compound, drug	Polyethylene glycol		SigmaMillipore	25322-68-3	
chemical compound, drug	Uranyl acetate		Electron Microscopy Sciences	Cat#22400	
chemical compound, drug	Reynold's lead citrate		Electron Microscopy Sciences	#17800	
chemical compound, drug	Picrotoxin		SigmaMillipore	Cat# P1675	
chemical compound, drug	LY303070		ABX Chemical Co.	N/A	Custom Order
chemical compound, drug	MK-801		Tocris Bioscience	Cat# 0924	
chemical compound, drug	DCG-IV		Tocris Bioscience	Cat# 0975	
chemical compound, drug	D-APV		Tocris Bioscience	Cat# 0106	

chemical compound, drug	D-APV	NIMH Chemical Synthesis Program	N/A	
chemical compound, drug	R-CPP	Tocris Bioscience	Cat# 0247	
chemical compound, drug	NBQX	Cayman Chemical Co.	Cat# 14914	
chemical compound, drug	Fluo5-F pentapotassium salt cell impermeant	Invitrogen Molecular Probes	Cat# F14221	
chemical compound, drug	Alexa Fluor 594 Hydrazide	Invitrogen Molecular Probes	Cat# A10438	
chemical compound, drug	Alexa Fluor 488 Hydrazide	Invitrogen Molecular Probes	Cat# A10436	
chemical compound, drug	D-Serine	Tocris Bioscience	Cat# 0226	
chemical compound, drug	MNI-caged-L-glutamate	Tocris Bioscience	Cat# 1490	
chemical compound, drug	Sucrose	SigmaMillipore	Cat# S9378	
chemical compound, drug	KCl	SigmaMillipore	Cat# P3911	
chemical compound, drug	NaH_2PO_4	SigmaMillipore	Cat# S9638	
chemical compound, drug	$CaCl_2$	SigmaMillipore	Cat# C8106	

chemical compound, drug	$MgCl_2$	SigmaMillipore	Cat# M2670	
chemical compound, drug	$MgSO_4$	SigmaMillipore	Cat# M1880	
chemical compound, drug	Glucose	SigmaMillipore	Cat# G8270	
chemical compound, drug	NaCl	SigmaMillipore	Cat# S7653	
chemical compound, drug	$NaHCO_3$	SigmaMillipore	Cat# S6014	
chemical compound, drug	Cesium hydroxide	SigmaMillipore	Cat# 23204	
chemical compound, drug	D-gluconic acid	SigmaMillipore	Cat# G1951	
chemical compound, drug	EGTA	SigmaMillipore	Cat# E4378	
chemical compound, drug	HEPES	SigmaMillipore	Cat# H3375	
chemical compound, drug	Potassium gluconate	SigmaMillipore	Cat# G4500	
chemical compound, drug	MgATP	SigmaMillipore	Cat# A9187	
chemical compound, drug	Na_3GTP	SigmaMillipore	Cat# G0635	

chemical compound, drug	NMDG	SigmaMillipore	Cat# M2004	
chemical compound, drug	Sodium ascorbate	SigmaMillipore	Cat# A4034	
chemical compound, drug	Thiourea	SigmaMillipore	Cat# T8656	
chemical compound, drug	Sodium pyruvate	SigmaMillipore	Cat# P2256	
chemical compound, drug	$KMeSO_4$	SigmaMillipore	Cat# 83000	
chemical compound, drug	Na_2ATP	SigmaMillipore	Cat# A2383	
chemical compound, drug	NaGTP	SigmaMillipore	Cat# 51120	
chemical compound, drug	Sodium Phosphocreatine	SigmaMillipore	Cat# P7936	
chemical compound, drug	NH_4Cl	SigmaMillipore	Cat# A9434	
chemical compound, drug	KOH	EMD Millipore	Cat# 109108	
chemical compound, drug	HCl	Fisher Chemical	Cat# SA49	
software, algorithm	IgorPro7	Wavemetrics		https://www.wavemetrics.com/

software, algorithm	Origin Pro 9	Origin Lab		https://www.originlab.com/
software, algorithm	ImageJ	ImageJ		http://imagej.net/Welcome
software, algorithm	Multiclamp 700B	Molecular Devices		https://www.moleculardevices.com/
software, algorithm	Prairie View 5.4	Bruker Corp.		https://www.pvupdate.blogspot.com/

462

463 **Antibodies**

464 A monoclonal antibody against GluN1 (clone 54.1 MAB363) was obtained from Millipore
465 (Germany) and its specificity was characterized previously (Siegel et al., 1994). An affinity-purified
466 polyclonal rabbit anti-GluA1-4 (pan-AMPA), corresponding to aa 724–781 of rat, was used and
467 characterised previously (Nusser et al., 1998).

468

469 **Immunohistochemistry for electron microscopy**

470 Immunohistochemical reactions at the electron microscopic level were carried out using the post-
471 embedding immunogold method as described earlier (Lujan et al., 1996). Briefly, animals (n = 3
472 rats were anesthetized by intraperitoneal injection of ketamine-xylazine 1 : 1 (0.1 mL/kg b.w.) and
473 transcardially perfused with ice-cold fixative containing 4% paraformaldehyde, 0.1%
474 glutaraldehyde and 15% saturated picric acid solution in 0.1 M phosphate buffer (PB) for 15 min.
475 Vibratome sections 500 μm thick were placed into 1 M sucrose solution in 0.1 M PB for 2 h before
476 they were slammed on a Leica EM CPC apparatus. Samples were dehydrated in methanol at -
477 80°C and embedded by freeze-substitution (Leica EM AFS2) in Lowicryl HM 20 (Electron
478 Microscopy Science, Hatfield, USA), followed by polymerization with UV light. Then, ultrathin 80-

479 nm-thick sections from Lowicryl-embedded blocks of the hippocampus were picked up on coated
480 nickel grids and incubated on drops of a blocking solution consisting of 2% human serum albumin
481 in 0.05 M TBS and 0.03% Triton X-100. The grids were incubated with GluN1 or pan-AMPA
482 antibodies (10 µg/mL in 0.05 M TBS and 0.03% Triton X-100 with 2% human serum albumin) at
483 28 °C overnight. The grids were incubated on drops of goat anti-rabbit IgG conjugated to 10 nm
484 colloidal gold particles (Nanoprobes Inc.) in 2% human serum albumin and 0.5% polyethylene
485 glycol in 0.05 M TBS and 0.03% Triton X-100. The grids were then washed in TBS and
486 counterstained for electron microscopy with 1% aqueous uranyl acetate followed by Reynolds's
487 lead citrate. Ultrastructural analyses were performed in a JEOL-1010 electron microscope.
488

489 **Hippocampal slice preparation**

490 Animal handling followed an approved protocol by the Albert Einstein College of Medicine
491 Institutional Animal Care and Use Committee in accordance with the National Institute of Health
492 guidelines. Acute rat hippocampal slices (400 µm thick) were obtained from Sprague-Dawley
493 rats, from postnatal day 17 (P17) to P28 of either sex. For procedures regarding transgenic mouse
494 slice preparation, see below. The hippocampi were isolated and cut using a VT1200s microslicer
495 (Leica Microsystems Co.) in a solution containing (in mM): 215 sucrose, 2.5 KCl, 26 $NaHCO_3$, 1.6
496 NaH_2PO_4, 1 $CaCl_2$, 4 $MgCl_2$, 4 $MgSO_4$ and 20 glucose. Acute slices were placed in a chamber
497 containing a 1:1 mix of sucrose cutting solution and normal extracellular artificial cerebrospinal
498 fluid (ACSF) recording solution containing (in mM): 124 NaCl, 2.5 KCl, 26 $NaHCO_3$, 1 NaH_2PO_4,
499 2.5 $CaCl_2$, 1.3 $MgSO_4$ and 10 glucose incubated in a warm-water bath at 33-34 ºC. The chamber
500 was brought to room temperature for at least 15 min post-sectioning and the 1:1 sucrose-ACSF
501 solution was replaced by ACSF. All solutions were equilibrated with 95% O_2 and 5% CO_2 (pH
502 7.4). Slices were allowed to recover for at least 45 min in the ACSF solution before recording.
503 For physiological Mg^{+2} and Ca^{+2} experiments, ACSF solutions were adjusted to (in mM): 1.2
504 $MgSO_4$, and 1.2 $CaCl_2$ and temperature was maintained at 35 ± 0.1 °C in the submersion-type

505 recording chamber heated by a temperature controller (TC-344B Dual Automatic Temperature
506 Controller, Warner Instruments).
507
508 **Electrophysiology**
509 Electrophysiological recordings were performed at 26.0 ± 0.1 ºC (unless otherwise stated) in a
510 submersion-type recording chamber perfused at 2 mL/min with normal ACSF supplemented with
511 the $GABA_A$ receptor antagonist picrotoxin (100 μM) and the selective AMPA receptor (AMPAR)
512 antagonist LY303070 at a low concentration (0.5 μM) to minimize CA3-CA3 recurrent activity, or
513 at a high concentration (15 μM) to isolate KAR-EPSCs and KAR-EPSPs to assess monosynaptic
514 mf transmission. Whole-cell recordings were made from CA3 pyramidal cells voltage clamped at
515 -70 mV using patch-type pipette electrodes (3-4 mΩ) containing (in mM): 131 cesium gluconate,
516 8 NaCl, 1 $CaCl_2$, 10 EGTA, 10 glucose, 10 HEPES, and 2 MK-801 pH 7.25 (280-285 mOsm)
517 unless specified otherwise. KOH was used to adjust pH. Series resistance (8-15 MΩ) was
518 monitored throughout all experiments with a -5 mV, 80 ms voltage step, and cells that exhibited a
519 series resistance change (>20%) were excluded from analysis. A stimulating bipolar electrode
520 (theta glass, Warner Instruments) was filled with ACSF and placed in *stratum lucidum* to
521 selectively activate mfs using a DS2A Isolated Voltage Stimulator (Digitimer Ltd.) with a 100 μs
522 pulse width duration. AMPAR-EPSCs were recorded for a baseline period of two minutes and
523 low-frequency facilitation (LFF) was induced by stepping the stimulation frequency from 0.1 to 1
524 Hz for two minutes. Facilitation was measured by taking a ratio of the mean EPSC during the
525 steady-state, LFF period of activity and the two-minute baseline ($EPSC_{1Hz}/EPSC_{0.1Hz}$) before and
526 after bath-application of NMDAR antagonists.
527
528 To qualify for analysis, mf responses met three criteria: 1) The 20-80% rise time of the AMPAR-
529 EPSC was less than 1 ms, 2) LFF was greater than 150%, 3) The AMPAR-EPSC displayed at
530 least 70% sensitivity to the group 2/3 mGluR agonist, DCG-IV (1 μM). Isolated KAR-EPSCs were

531 elicited by 2 pulses with a 5 ms inter-stimulus-interval for LFF experiments. Baseline
532 measurements were acquired at least 10 min after "break-in" to achieve optimal intracellular
533 blockade of postsynaptic NMDARs by MK-801 (2 mM) in the patch-pipette. To transect mf axons
534 in acute slices, a 45° ophthalmic knife (Alcon Surgical) was used to make a diagonal cut across
535 the hilus from the dorsal to ventral blades of the DG, and the subregion CA3b was targeted for
536 patch-clamp recordings. For D-APV (2 mM) puff experiments, a puffer device (Toohey Company)
537 was set to deliver 2-3 puffs of 100 ms duration at 3-4 psi during the two minutes of LFF activity.
538 The puffer pipette was placed at least 200 μm away from the recording site and both the puff
539 pipette and hippocampal slice were positioned to follow the direction of the laminar perfusion flow
540 in a low profile, submersion-type chamber (RC-26GLP, Warner Instruments). Burst-induced
541 facilitation was elicited by 5 pulses at 25 Hz with a 0.03 Hz inter-trial-interval for a baseline period
542 of 10 min. Facilitation was measured by calculating the ratio of the mean KAR-EPSC peak of the
543 5th pulse to the 1st pulse (P_5/P_1) before and after bath-application of MK-801 (50 μM). To study
544 KAR induced action potentials, CA3 pyramidal cells were whole-cell patch-clamped with internal
545 solution containing in (mM): 112 potassium gluconate, 17 KCl, 0.04 $CaCl_2$, 0.1 EGTA, 10 HEPES,
546 10 NaCl, 2 MgATP, 0.2 Na_3GTP and 2 MK-801, pH 7.2 (280-285 mOsm). Current-clamped CA3
547 cells were held at -70 mV during burst stimulation of mfs (5 pulses at 25 Hz) to monitor evoked
548 action potentials. Spike-transfer was measured by quantifying mean number of spikes/burst for
549 a 10 min period before and after bath application of MK-801 (50 μM). Robust sensitivity to the
550 AMPAR/KAR selective antagonist NBQX (10 μM) confirmed KAR-EPSC responses. Similarly,
551 CA3 pyramidal cells were kept in current-clamp mode for AMPAR-mediated action potential
552 monitoring in the presence of LY303070 (0.5 μM) and picrotoxin (100 μM). AMPAR-mediated mf
553 action potentials were confirmed by blockade of responses following application of DCG-IV (1
554 μM). Both hilar mossy cells and CA3 interneurons were visually patched-loaded with Alexa 594
555 (35 μM) and morphological identity was confirmed by two-photon laser scanning imaging at the
556 end of experiments. Hilar mossy cells were voltage clamped at -70 mV and a bipolar electrode

557 was placed in the DG to activate mf inputs. The data analysis and inclusion criteria used for mf
558 experiments (described above) was also implemented for hilar mossy cell recordings. CA3
559 interneurons were voltage clamped at -70 mV and burst-stimulated, facilitation was assessed as
560 previously mentioned. Both facilitating and depressing mf responses were included for analysis
561 given the diversity of mf-CA3 interneuron transmission (Toth et al., 2000). Whole-cell voltage and
562 current clamp recordings were performed using an Axon MultiClamp 700B amplifier (Molecular
563 Devices). Signals were filtered at 2 kHz and digitized at 5 kHz. Stimulation and acquisition were
564 controlled with custom software (Igor Pro 7).
565
566 **Transgenic animals**
567 *Grin1*-floxed littermate mice of either sex (P16-20) were injected with 1 µL of AAV5-CamKII-eGFP,
568 AAV5-CamKII-CreGFP, AAV5-CamKII-mCherry, or AAV5-CamKII-mCherry-Cre viruses at a rate
569 of 0.12 µL/min at coordinates (-1.9 mm A/P, 1.1 mm M/L, 2.4 mm D/V) targeting the DG using a
570 stereotaxic apparatus (Kopf Instruments). Two weeks post-surgery mice were sacrificed for
571 electrophysiology or Ca^{2+} imaging experiments. Mice were transcardially perfused with 20 mL of
572 cold NMDG solution containing in (mM): 93 NMDG, 2.5 KCl, 1.25 NaH_2PO_4, 30 $NaHCO_3$, 20
573 HEPES, 25 glucose, 5 sodium ascorbate, 2 Thiourea, 3 sodium pyruvate, 10 $MgCl_2$, 0.5 $CaCl_2$,
574 brought to pH 7.35 with HCl. The hippocampi were isolated and cut using a VT1200s microslicer
575 in cold NMDG solution. Acute mouse slices were placed in an incubation chamber containing
576 normal ACSF solution that was kept in a warm water bath at 33-34 ˚C. All solutions were
577 equilibrated with 95% O_2 and 5% CO_2 (pH 7.4). Post-sectioning, slices recovered at room
578 temperature for at least 45 min prior to experiments. For NMDAR/AMPAR ratios, GCs were patch-
579 clamped with the cesium internal solution previously mentioned containing either Alexa 594 (35
580 µM) for GFP^+ cells (laser tuned to 830 nm/910 nm, respectively) or Alexa 488 (35 µM) for
581 $mCherry^+$ cells (laser tuned to 910 nm/780 nm, respectively). AMPAR-EPSCs were recorded at -
582 65 mV in the presence of picrotoxin (100 µM) by placing a bipolar electrode near the medial

583 perforant path and delivering a 100 μs pulse width duration using an Isoflex stimulating unit.
584 AMPAR-EPSCs were acquired for at least 5 min followed by bath-application of NBQX (10 μM)
585 to isolate NMDAR-EPSCs. GCs were brought to +40 mV to alleviate magnesium block and record
586 optimal NMDAR-EPSCs. NMDAR/AMPAR ratios were measured by taking the mean NMDAR-
587 EPSC/AMPAR-EPSC for a 5 min period of each component. Only acute mouse slices with
588 optimal GFP and mCherry reporter fluorescence (i.e. robust expression, ≥ 75% of dentate gyrus
589 fluorescence) were used for electrophysiology, and Ca^{2+} and BDNF imaging experiments. *Grin1*-
590 floxed animals (The Jackson Laboratory) were kindly provided by Dr. Michael Higley (Yale
591 University).
592
593 **Optogenetics**
594 *Grin1* floxed and control mice of either sexes (P17-20) were injected with a 1:2 mix of AAV5-
595 CamKII-CreGFP/AAV-DJ-FLEX-ChIEF-tdTomato viruses targeting the DG, using the same
596 coordinates described above. At least four weeks post-surgery acute hippocampal slices were
597 prepared as previously described and slices showing optimal GFP and tdTomato expression were
598 used for electrophysiology experiments. Mf optical burst-stimulation was elicited by using a
599 Coherent 473 nm laser (4-8 mW) delivering 5 pulses at 25 Hz with a 1-2 ms pulse width duration.
600 Facilitation was measured by taking a ratio of the mean AMPAR-EPSC peak of the 5th pulse to
601 the 1st pulse (P_5/P_1) in control and *Grin1*-cKO animals.
602
603 **Two-photon calcium imaging and MNI-glutamate uncaging**
604 mCherry+ GCs were patch-loaded with an internal solution containing in (mM): 130 $KMeSO_4$, 10
605 HEPES, 4 $MgCl_2$, 4 Na_2ATP, 0.4 NaGTP, 10 sodium phosphocreatine, 0.035 Alexa 594 (red
606 morphological dye), and 0.2 Fluo-5F (green calcium indicator), 280-285 mOsm. KOH was used
607 to adjust pH. GCs near the hilar border were avoided and GCs that exhibited adult-born GCs
608 electrophysiological properties were excluded from analysis. GCs were kept in voltage clamp

609 configuration at -50 mV for at least 1 hr to allow the diffusion of dyes to mf boutons. Recordings
610 were obtained in ACSF solution containing in (mM): 124 NaCl, 2.5 KCl, 26 $NaHCO_3$, 1 NaH_2PO_4,
611 4 $CaCl_2$, 0 $MgSO_4$, 10 glucose, 0.01 NBQX, 0.1 picrotoxin, and 0.01 D-serine. Using an Ultima
612 2P laser scanning microscope (Bruker Corp) equipped with an Insight Deep See laser (Spectra
613 Physics) tuned to 830 nm, the "red" photomultiplier tube (PMT) was turned on and with minimal
614 pockel power the red signal was used to identify the mf axon. With 512 x 512 pixel resolution mf
615 axons were followed for at least 200 µm from the DG towards CA3, until bouton structures were
616 morphologically identified and measured (>3 µm in diameter). GCs were switched to current
617 clamp mode held at -70 mV and 1 ms current injections were used to elicit a burst of 5 action
618 potentials at 25 Hz. Using line scan analysis software (PrairieView 5.4, Bruker Corp.), a line was
619 drawn across the diameter of the bouton at a magnification of at least 16X. The “green” PMT
620 channel was turned on and 1,000 line scans were acquired in a 2 s period. Action potential
621 induction was delayed for 400 ms to collect a baseline fluorescence time period. Calcium
622 transients (CaTs) were acquired with a 1 min inter-trial-interval and analyzed using the ΔG/R
623 calculation: $(G - G_0)/R$. CaTs from control animals were compared to *Grin1*-cKO by taking the
624 mean peak ΔG/R value for a 30 ms period of the 5th action potential. In similar fashion, CaT
625 signals in acute rat hippocampal slices were acquired and tested for sensitivity to D-APV (100
626 µM) while adjusting ACSF $MgS0_4$ concentration to 1.3 mM and $CaCl_2$ to 2.5 mM in the absence
627 of NBQX.
628
629 For glutamate uncaging experiments, GCs that were mCherry+ were patch-loaded using the
630 internal solution previously described, and a small volume (12 mL) of recirculated ACSF solution
631 containing in (mM): 124 NaCl, 2.5 KCl, 26 $NaHCO_3$, 1 NaH_2PO_4, 4 $CaCl_2$, 0 $MgSO_4$, 10 glucose,
632 2.5 MNI-glutamate, 0.01 NBQX, 0.1 picrotoxin, and 0.01 D-serine. A MaiTai HP laser (Spectra
633 Physics) was tuned to 720 nm to optimally uncage glutamate and elicit CaTs in GC dendritic
634 spines. Following the measurement of CaTs in GC spines, mf boutons were identified and to

635 mimic bursting activity, 5 uncaging pulses (1 ms duration) were delivered at 25 Hz. The acquired
636 CaTs in spines and boutons were analyzed using the ΔG/R calculation in control and *Grin1*-cKO
637 animals. In a subset of control boutons, D-APV (100 μM) was applied to detect CaT sensitivity to
638 NMDAR antagonism.
639
640 **Two-photon BDNF-phluorin imaging**
641 *Grin1* floxed and control mice of both sexes (P16-20) were injected with a 1:2 mix of AAV5-
642 CamKII-mCherryCre/AAV-DJ-DIO-BDNF-phluorin viruses targeting the DG using the same
643 coordinates as above. At least four weeks post-surgery acute hippocampal slices were prepared
644 as previously described and slices showing optimal GFP and mCherry expression were taken for
645 imaging sessions. For stimulation, a monopolar micropipette electrode was placed in the *stratum*
646 *lucidum* at least 250 μm away from the imaging site. The Insight Deep See laser (Spectra
647 Physics) was tuned to 880 nm and the imaging site was selected by the appearance of fibers and
648 bouton structures in the *stratum lucidum*. Using 512 X 512 pixel resolution identified boutons
649 measuring at least 3 μm in diameter were selected as a region of interest (ROI) magnified to 4-
650 6X and a baseline acquisition of 100 consecutive images at 1 Hz using T-series software
651 (PrairieView 5.4, Bruker Corp.) was acquired (Park et al., 2014). Following the baseline
652 acquisition a repetitive stimulation consisting of 125 pulses at 25 Hz was delivered 2x, triggering
653 an acquisition of 200 consecutive images at 1 Hz. The fluorescence intensity of the bouton ROI
654 was measured using ImageJ software to calculate ΔF/F of the BDNF-pHluorin signal. To verify
655 reactivity of the ROI an isosmotic solution of NH_4Cl (50 mM) was added at the end of the imaging
656 session as previously reported (Park et al., 2014). The same experimental and analysis procedure
657 was implemented to measure BDNF release triggered by mf burst stimulation consisting of 5
658 pulses at 100 Hz, 50x, every 0.5 s.
659
660 **Viruses**

661 AAV5-CamKII-eGFP and AAV5-CamKII-CreGFP viruses were acquired from UPenn Vector Core.
662 AAV5-CamKII-mCherry and AAV5-CamKII-mCherry-Cre were obtained from UNC Chapel Hill
663 Vector Core. The AAV-DJ-FLEX-ChIEF-tdTomato and AAV-DJ-DIO-BDNF-phluorin viruses were
664 custom ordered and obtained from UNC Chapel Hill Vector Core. The DNA of the ChIEF virus
665 was a generous gift from Dr. Pascal Kaeser (Harvard University), and the DNA of the BDNF-
666 pHluorin was kindly provided by Dr. Hyungju Park (Korea Brain Research Institute).
667
668 **Chemicals & Drugs**
669 Picrotoxin and all chemicals used to prepare cutting, recording, and internal solutions were
670 acquired from MilliporeSigma. All NMDAR antagonists (D-APV, MK-801, R-CPP), NMDAR
671 agonist (D-serine), the group 2/3 mGluR agonist (DCG-IV) and MNI-glutamate for uncaging
672 experiments were purchased from Tocris Bioscience. D-APV was also acquired from the NIMH
673 Chemical Synthesis Drug Program. NBQX was purchased from Cayman Chemical Company.
674 The noncompetitive AMPAR selective antagonist LY303070 was custom ordered from ABX
675 Chemical Company. Alexa 594 morphological dye, Alexa 488, and the Ca^{2+} indicator Fluo-5F
676 (Invitrogen) were purchased from ThermoFisher Scientific.
677
678 **Statistical analysis and Data Acquisition**
679 All data points from experiments were tested for normality using a Shapiro-Wilk test (p value <
680 5% for a normal distribution). Statistical significance was determined if p value < 0.05.
681 Experiments with a normal distribution and an N > to 7 cells were tested for statistical significance
682 with a paired Student *t*-test. Experiments with N < 7 cells or skewed distributions were tested for
683 statistical significance using a paired Wilcoxon signed rank sum test. For experiments comparing
684 control and *Grin1*-cKO animals, statistical significance was determined using Unpaired *t*-test and
685 Mann-Whitney test (U < 0.05). All statistical tests were performed using Origin Pro 9 (Origin Lab).
686 Experimenters were blind to the identity of the virus injected in transgenic *Grin1* floxed mice during

687 the acquisition of data in CA3 electrophysiology and two-photon imaging. However, data analysis
688 could not be performed blind in those experiments in which NMDAR/AMPAR ratios in GCs were
689 examined in order to assess the efficiency of the cKO.
690

691

692 **Figure Legends**

693 **Figure 1. Anatomical and functional evidence for preNMDARs at mossy fiber synapses.** (**A**)
694 Image of a mossy fiber (mf) giant bouton and postsynaptic spines (s). (**B, C**) Higher magnification
695 of mf synapses. Arrows indicate postsynaptic GluN1 whereas arrowheads indicate presynaptic
696 GluN1. Calibration bars: 500 nm. (**D**) Mossy fiber (mf) and associational commissural (ac)
697 synaptic GluN1 immuno-particle radial distribution (30 nm bins), mf: 34 synapses, 100 presynaptic
698 particles; ac: 25 synapses, 24 presynaptic particles; 3 animals. (**E**) AMPAR-ESPCs were
699 recorded at V_h= -70 mV in the presence of 0.5 μM LY303070 and 100 μM picrotoxin. Low-
700 frequency facilitation (LFF), induced by stepping stimulation frequency from 0.1 to 1 Hz, was
701 assessed before and after bath application of MK-801 (50 μM). MK-801 significantly reduced LFF
702 (baseline 378 ± 57%, MK-801 270 ± 48%, n = 10 cells, 9 animals; baseline vs MK-801, p = 3.8 x
703 10^{-5}, paired *t*-test). In all panels of this figure: representative traces (*top*), representative
704 experiment (*middle*), normalized LFF and summary plot (*bottom*). DCG-IV (1 μM) was applied at
705 the end of all recordings to confirm mf-CA3 transmission. (**F**) D-APV (100 μM) or R-CPP (50 μM)
706 application also reduced LFF (baseline 546 ± 50%, D-APV/R-CPP 380 ± 38%, n = 7 cells, 5
707 animals; baseline vs D-APV/R-CPP, p = 0.00743, paired *t*-test). (**G**) KAR-EPSCs were recorded
708 at V_h= -70 mV in the presence of 15 μM LY303070 and 100 μM picrotoxin. In addition, NMDAR-
709 mediated transmission was blocked intracellularly by loading MK-801 (2 mM) in the patch-pipette.
710 Bath application of MK-801 (50 μM) significantly reduced LFF (baseline 278 ± 40%, MK-801 195
711 ± 26% n = 8 cells, 6 animals; baseline vs MK-801, p = 0.00259, paired *t*-test). Data are presented
712 as mean ± s.e.m. ** p < 0.01; *** p < 0.005; **** p < 0.001.

713

714 **Supplementary Figure 1 related to Figure 1**. Immunogold-EM reveals negligible presynaptic
715 AMPAR particle distribution. (**A,B**) Images of mossy fiber (mf) and associational commissural (ac)
716 synapses, postsynaptic spines (s). (**C**) AMPAR immuno-particle distribution (30 nm bins), mf: 102

717 synapses, 8 presynaptic particles; ac: 75 synapses, 6 presynaptic particles; 3 animals. Dashed
718 line represents synaptic cleft.
719
720 **Supplementary Figure 2 related to Figure 1.** (**A**) Stable low-frequency facilitation (LFF) of
721 AMPAR-EPSCs. In naïve slices (interleaved experiments), LFF remained unchanged throughout
722 the recording session (baseline 335 ± 62%, naïve 363 ± 63%, n = 10 cells, 9 animals; p = 0.185,
723 Wilcoxon-Signed Ranks test, baseline vs naÏve). DCG-IV (1 μM) was applied at the end of all
724 recordings to confirm mf-CA3 transmission. (**B**) LFF of KAR-EPSCs was also stable in
725 interleaved, naïve slices (baseline 274 ± 33%, naïve 278 ± 25%, n = 9 cells, 6 animals; p = 0.236,
726 Wilcoxon Signed Ranks test, baseline vs naïve). NBQX (10 μM) was applied at the end of all
727 recordings to confirm mf KAR transmission. Data are presented as mean ± s.e.m.
728
729 **Figure 2. GluN1 deletion from granule cells reduces mf-CA3 facilitation.** (**A**) Representative
730 images showing GCs patch-loaded with Alexa 594 (35 μM) *(left),* and GFP expression in GCs
731 *(right)*. (**B**) Representative EPSCs recorded from control (GFP^+) and *Grin1*-cKO (Cre-GFP^+) GCs.
732 Synaptic responses were elicited by activating medial perforant-path inputs. AMPAR-ESPCs were
733 recorded at V_h= -65 mV in the presence of 100 μM picrotoxin, NMDAR-EPSCs were isolated with
734 10 μM NBQX and recorded at +40 mV. MK-801 (20 μM) was applied at the end of each recording.
735 (**C**) Summary plot demonstrating that GluN1 deletion from GCs virtually abolished NMDAR-
736 mediated transmission indicated by a strong reduction of NMDAR/AMPAR in *Grin1*-cKO GCs as
737 compared to controls (control 1.61 ± 0.18, n = 9 cells, 9 animals, *Grin1*-cKO 0.18 ± 0.04, n = 10
738 cells, 10 animals; control vs *Grin1*-cKO, p = 9.2 x 10^{-6}, unpaired *t*-test). (**D**) LFF was significantly
739 reduced in GluN1-deficient animals (control, 430 ± 5 %, n = 13 cells, 10 animals; *Grin1*-cKO, 291
740 ± 6 %, n = 11 cells, 10 animals; p = 0.0239, unpaired *t*-test). Representative traces (*left*) and
741 summary plot (*right*). LFF was induced by stepping stimulation frequency from 0.1 to 1 Hz. DCG-
742 IV (1 μM) was added at the end of each experiment. Data are presented as mean ± s.e.m. * p <

743 0.05; **** $p < 0.001$.

744

745 **Figure 3. Reduced facilitation by NMDAR antagonism is independent of the GC**
746 **somatodendritic compartment.** (**A**) KAR-EPSCs were recorded at V_h= -70 mV in the presence
747 of 15 μM LY303070 and 100 μM picrotoxin. In addition, NMDAR-mediated transmission was
748 blocked intracellularly by loading MK-801 (2 mM) in the patch-pipette. LFF of KAR-EPSCs was
749 assessed as in Fig. 1G but with transected mf axons (see Methods). Bath application of MK-801
750 (50 μM) significantly reduced LFF (baseline 213 ± 9%, MK-801 181 ± 10%, n = 8 cells, 7 animals;
751 baseline vs MK-801, p = 0.002, paired *t*-test). In all panels of this figure: recording arrangement
752 (*inset*), representative traces (*top*), representative experiment (*middle*), normalized LFF and
753 summary plot (*bottom*). (**B**) Stable LFF in transected, naïve slices (baseline 186 ± 10%, naïve
754 196 ± 5%, n = 8 cells, 7 animals; baseline vs naïve, p = 0.278, paired *t*-test). (**C**) LFF was induced
755 before and during puff application of D-APV (2 mM) in *stratum lucidum*. This manipulation
756 significantly reduced facilitation (baseline 220 ± 19%, D-APV puff 176 ± 11%, n = 7 cells, 7
757 animals; baseline vs D-APV puff, p = 0.003, paired *t*-test). (**D**) Stable LFF in acute slices during
758 puff application of ACSF (baseline 210% ± 12, naïve 213% ± 9, n = 7 cells, 7 animals; baseline
759 vs naïve, p = 0.778, paired *t*-test). NBQX (10 μM) was applied at the end of all recordings to
760 confirm mf KAR transmission. Data are presented as mean ± s.e.m. *** $p < 0.005$.

761

762 **Supplementary Figure 3 related to Figure 3.** Targeting preNMDARs located in mf axons but not
763 granule cells. (**A**) Field view of a representative hippocampal slice showing a surgical cut between
764 DG and CA3. (**B**) Local D-APV puff application (vertical arrow, 2 puffs at 0.1 Hz) blocks NMDAR
765 currents recorded at V_h= -50 mV and washes out in less than 10 minutes (n = 7 cells, 5 animals,
766 $p = 5 \times 10^{-8}$, paired *t*-test). Inset depicts the recording paradigm of the experiment *(left)*, the
767 representative NMDAR currents *(top)* and the summary time course *(bottom)* where arrows
768 denote the onset of D-APV (2 mM) puff application. Mfs were stimulated with a bipolar electrode

769 (theta-glass pipette) in *stratum lucidum* in the presence of 100 μM picrotoxin and 10 μM NBQX.
770 (**C**) D-APV puff application in CA3 did not reduce NMDAR transmission in GCs (n = 6 cells, 5
771 animals, control vs D-APV puff, U = 0.594, Mann Whitney test). Excitatory inputs were stimulated
772 with a monopolar electrode placed in the medial molecular layer/inner molecular layer, in the
773 presence of 100 μM picrotoxin and 10 μM NBQX, while GCs were clamped at V_h= +40 mV. Data
774 are presented as mean ± s.e.m.
775
776 **Figure 4. PreNMDARs contribute significantly to burst-induced facilitation and spike**
777 **transfer.** (**A**) Representative images showing expression of GFP-Cre *(left)* and ChIEF-tdTomato
778 *(right)* in the DG of control and *Grin1*-cKO animals. (**B**) Representative AMPAR-EPSCs from
779 control *(left)* and *Grin1*-cKO *(right)* CA3 pyramidal neurons recorded at V_h= -65 mV and evoked
780 by optical burst-stimulation (5 pulses at 25 Hz) of *stratum lucidum*. Blue arrows indicate light
781 stimulation. (**C**) Summary plot of burst-induced facilitation measured as P5/P1 ratio of optical
782 responses; facilitation was significantly reduced in *Grin1*-cKO animals as compared to control
783 (*Grin1*-cKO 187 ± 16%, n = 12 cells, 9 animals; control 255 ± 22%, n = 9 cells, 8 animals; *Grin1*-
784 cKO vs control, p = 0.0167, unpaired *t*-test). (**D**) Burst-stimulation induced KAR-EPSCs were
785 isolated and recorded as described in Fig. 3, bath-application of MK-801 (50 μM) significantly
786 reduced facilitation (baseline 601 ± 107%, MK-801 464 ± 84%, n = 13 cells, 10 animals; baseline
787 vs MK-801, p = 0.00042, paired *t*-test). In panels D and E of this figure: representative traces
788 (*left*), representative experiment (*middle*), and summary plot (*right*). (**E**) Burst-induced facilitation
789 was stable in interleaved, naïve slices (baseline 369 ± 45%, naïve 367 ± 48%, n = 9 cells, 9
790 animals; p = 0.863, paired *t*-test). (**F**) Bath-application of MK-801 (50 μM) reduced KAR-mediated
791 action potentials induced by burst-stimulation (baseline 0.93 ± 0.17, MK-801 0.46 ± 0.09, n = 6
792 cells, 5 animals; p = 0.036, Wilcoxon Signed Ranks test). In panels F and G of this figure:
793 representative traces (*top)*, representative experiment and summary plot (*bottom)*. (**G**) Stable
794 KAR-mediated action potentials in interleaved naïve slices (baseline 0.76 ± 0.07, naïve 0.88 ±

795 0.1, n = 6 cells, 5 animals; p = 0.2084, Wilcoxon Signed Ranks test). NBQX (10 μM) was applied
796 at the end of all experiments in panels D-G. Data are presented as mean ± s.e.m. * $p < 0.05$; ****
797 $p < 0.001$.
798
799 **Supplementary Figure 4 related to Figures 1 & 4.** Intracellular MK-801 effectively blocked
800 postsynaptic NMDARs. In each panel of this figure, representative NMDAR-EPSCs from CA3
801 pyramidal neurons patch-loaded with 2 mM MK-801 *(left)* or naïve internal solution *(right)*. Mf
802 inputs were stimulated with a bipolar electrode (theta-glass pipette) in *stratum lucidum* delivering
803 1 pulse or 5 pulses at 25 Hz in the presence of picrotoxin (100 μM) and NBQX (10 μM). (**A**)
804 NMDAR currents were recorded at V_h = + 40 mV in intracellular MK-801 (iMK-801) and naïve
805 conditions. Bath-application of MK-801 (50 μM) blocked NMDAR currents in naïve cells to a
806 similar magnitude as cells patch-loaded with MK-801 (n = 5 cells, 4 animals in each condition; U
807 = 0.676, Mann-Whitney test). Note that CA3 pyramidal neurons were loaded for at least 3-5
808 minutes before recording started at +40 mV. (**B**) NMDAR currents were recorded at V_h= + 40 mV
809 *(gray shaded area)* followed by a voltage jump to -70 mV in iMK-801 conditions and -50 mV in
810 naïve recordings. Bath-application of MK-801 (50 μM) blocked NMDAR currents of the 5th pulse
811 to a similar magnitude as iMK-801 (n = 5 cells, 4 animals per condition; U = 0.21, Mann-Whitney
812 test). Data are presented as mean ± s.e.m.
813
814 **Supplementary Figure 5 related to Figure 4.** PreNMDARs contribute to burst-induced
815 facilitation in more physiological conditions: 1.2 mM Mg^{+2}, 1.2 mM Ca^{+2} and 35 ºC. KAR-EPSCs
816 were recorded from CA3 pyramidal cells loaded with 2 mM MK-801 in the presence of 15 μM
817 LY303070 and 100 μM picrotoxin. (**A**) Bath-application of MK-801 (50 μM) significantly reduced
818 burst-induced facilitation elicited by 5 pulses, 25 Hz (baseline 450 ± 67%, MK-801 366 ± 63%, n
819 = 6 cells, 4 animals; baseline vs MK-801, p = 0.036, Wilcoxon Signed Ranks test). In panels A
820 and B of this figure: representative traces (*left*), representative experiment (*middle*), and summary

821 plot (*right*). (**B**) Burst-induced facilitation was stable in interleaved, naïve slices (baseline 462 ±
822 63%, naïve 481 ± 71%, n = 5 cells, 4 animals; p = 0.281, Wilcoxon Signed Ranks test). Data are
823 presented as mean ± s.e.m. * p < 0.05.
824
825 **Supplementary Figure 6 related to Figure 4.** PreNMDARs contribute to action potential firing
826 elicited by AMPAR-mediated transmission. (**A**) Bath-application of MK-801 (50 μM) reduced
827 action potentials induced by 5 pulses at 25 Hz burst-stimulation (baseline 2.47 ± 0.27, MK-801
828 1.9 ± 0.24, n = 6 cells, 5 animals; p = 0.036, Wilcoxon Signed Ranks test). In panels A and B of
829 this figure: representative traces (*top)*, representative experiment and summary plot (*bottom)*. (**B**)
830 Stable action potential firing in interleaved naïve slices (baseline 1.55 ± 0.24, naïve 1.61 ± 0.23,
831 n = 6 cells, 5 animals; p = 0.402, Wilcoxon Signed Ranks test). DCG-IV (1 μM) was applied at the
832 end of all experiments in panels A-B. Data are presented as mean ± s.e.m. * p < 0.05.
833
834 **Figure 5. preNMDARs contribute to presynaptic Ca^{2+} rise.** (**A**) Representative images showing
835 GCs patch-loaded with Alexa 488 (35 μM) to confirm expression of mCherry *(bottom)*.
836 Representative AMPAR-EPSCs recorded from control *(top)* or *Grin1*-cKO *(middle)* GCs. Synaptic
837 responses were elicited by activating medial perforant-path inputs. AMPAR-ESPCs were recorded
838 at V_h= -65 mV in the presence of 100 μM picrotoxin, NMDAR-EPSCs were isolated with 10 μM
839 NBQX and recorded at +40 mV. MK-801 (20 μM) was applied at the end of each experiment.
840 Summary plot *(bottom)* demonstrating that GluN1 deletion from GCs virtually abolished NMDAR-
841 mediated transmission indicated by a strong reduction of NMDAR/AMPAR in *Grin1*-cKO granule
842 cells as compared to controls (control 0.90 ± 0.17, n = 7 cells, 6 animals; *Grin1*-cKO 0.13 ± 0.05,
843 n = 6 cells, 6 animals; control vs *Grin1*-cKO, p = 3.81 x 10^{-7}, unpaired *t*-test). (**B**) Representative
844 control and *Grin1*-cKO GCs patch-loaded with Fluo-5F (200 μM) and Alexa 594 (35 μM). Arrows
845 indicate the identification of a mf giant bouton, magnified images in white box. (**C**) Three
846 representative mf boutons *(top)* and line scan analysis of calcium transients (CaTs) elicited by 5

847 action potentials at 25 Hz *(middle,* Fluo-5F*)* and morphological dye (*bottom*, Alexa 594), in Control
848 and *Grin1*-cKO animals. Dotted line (yellow) indicates line scan location. Red Channel, Alexa 594;
849 Green Channel, Fluo-5F. (**D, E**) Peak analysis of the 5th pulse ΔG/R revealed a significant
850 reduction in Ca^{2+} rise of *Grin1*-cKO animals as compared to Control (control 0.046 ± 0.01, n = 10
851 boutons, 8 animals; *Grin1*-cKO 0.025 ± 0.004, n = 10 boutons, 8 animals; control vs. *Grin1*-cKO,
852 U = 0.017, Mann-Whitney test). Arrows indicate mf activation. Data are presented as mean ±
853 s.e.m. * U < 0.05; **** p < 0.001.
854
855 **Supplementary Figure 7 related to Figure 5.** NMDAR antagonism reveals a reduction in
856 presynaptic Ca^{+2} rise in the presence of 1.3 mM Mg^{+2} and 2.5 mM Ca^{+2}. (**A, B**) Granule cells
857 were patch-loaded with Fluo-5F (200 μM) and Alexa 594 (35 μM). Line scan analysis of mf giant
858 bouton calcium transients (CaTs) in response to action potential (AP) stimulation (5 APs, 25 Hz).
859 (**C**) Line scan signals following D-APV application or naïve conditions. (**D**) D-APV (100 μM)
860 significantly reduced the 5th peak (P5) of CaTs (baseline 0.155 ± 0.04, D-APV 0.138 ± 0.03, n =
861 13 boutons, 10 animals; baseline vs D-APV, p = 0.00642, Wilcoxon Signed Ranks test). (**E**) In
862 naïve conditions P5 of CaTs is stable (baseline 0.104 ± 0.026, naïve 0.105 ± 0.026, n = 12
863 boutons, 10 animals; baseline vs naïve, p = 0.255, Wilcoxon Signed Ranks test). The first peak
864 (P1) of CaTs is not affected by D-APV (baseline 0.05 ± 0.017; D-APV 0.047 ± 0.014; baseline vs
865 D-APV, p = 0.485, Wilcoxon Signed Ranks test) and is stable in naïve conditions (baseline 0.033
866 ± 0.009; naïve 0.032 ± 0.009, baseline vs naïve, p = 0.196, Wilcoxon Signed Ranks test). Data
867 are presented as mean ± s.e.m. ** p < 0.01.
868
869 **Figure 6. Uncaging glutamate induces Ca^{2+} rise mossy fiber boutons.** (**A**) Representative
870 images showing dendritic spines in GCs *(left)* and mf boutons *(right),* and the associated line scan
871 analysis of calcium transients (CaTs) elicited by uncaging of MNI-glutamate (see Methods), in
872 control and *Grin1*-cKO animals. Blue dots indicate uncaging spots. Red Channel, Alexa 594;

873 Green Channel, Fluo-5F. (**B**) Line scan analysis of CaTs measuring ΔG/R in dendritic spines
874 when MNI-glutamate is uncaged in control or *Grin1*-cKO animals. Blue dots indicate location of
875 two photon uncaging (2PU) pulses. (**C**) Summary plot demonstrating a significant reduction in
876 dendritic spine CaTs in *Grin1*-cKO as compared to Control (control 0.053 ± 0.01 ΔG/R, n = 6
877 dendritic spines, 6 animals; *Grin1*-cKO 0.004 ± 0.003 ΔG/R, n = 6 spines, 6 animals; ΔG/R control
878 vs. *Grin1*-cKO, p = 0.00088, unpaired *t*-test). (**D**) Line scan analysis of CaTs measuring ΔG/R in
879 mf boutons when MNI-glutamate is uncaged in control or *Grin1*-cKO animals. (**E**) Summary plot
880 demonstrating significant CaTs in boutons of control as compared to *Grin1*-cKO (control 0.014 ±
881 0.005, n = 6 boutons, 6 animals; *Grin1*-cKO -0.00012 ± -0.0006, n = 6 boutons, 6 animals; control
882 vs. *Grin1*-cKO, p = 0.015, unpaired *t*-test). Data are presented as mean ± s.e.m. * p < 0.05; ****
883 p < 0.001.
884
885 **Supplementary Figure 8 related to Figure 6.** *Grin1*-cKO exhibit reduced CaTs at varying
886 uncaging laser power intensities. (**A**) Representative images of CaTs from control *(top)* and G*rin1*-
887 cKO animals *(bottom)* after MNI-glutamate uncaging (2 mM, 3 pulses at 25 Hz) on GC dendritic
888 spines. Dotted line (yellow) indicates line scan, and blue dots indicate 2PU spots. (**B**) Quantified
889 ΔG/R signals *(top)* and uncaging induced NMDAR-EPSCs *(bottom)* from control and *Grin1*-cKO
890 animals. Blue dots indicate when 2PU pulses were delivered. (**C**) Control animals display robust
891 ΔG/R signals as compared to *Grin1*-cKO animals at varying laser power intensities (6 spines, 6
892 animals per group, U = 0.00507 per power intensity, Mann-Whitney test). Data are presented as
893 mean ± s.e.m. ** U < 0.01.
894
895 **Supplementary Figure 9 related to Figure 6.** Bouton CaTs can be detected after repetitive
896 uncaging of MNI-glutamate. (**A**) Representative images of CaTs from single-trial: 1 pulse *(top)*
897 and 5 pulses, 25 Hz *(bottom)* of MNI-glutamate uncaging (2 mM). Dotted line (yellow) indicates
898 line scan, and blue dots indicate 2PU spots. (**B**) Quantified ΔG/R signals from 1 pulse *(black)* and

899 5 pulses *(dark gray)* from all trials. (**C**) Repetitive pulses result in larger ΔG/R signals as compared
900 to single pulses (n = 6 boutons, 6 animals, p = 0.03603, Wilcoxon-Signed Ranks test). Data are
901 presented as mean ± s.e.m. * p < 0.05.
902
903 **Supplementary Figure 10 related to Figure 6.** NMDAR antagonism with D-APV blocks CaTs
904 elicited by glutamate 2PU. (**A**) Representative image of baseline glutamate uncaging driven CaTs
905 in mf boutons *(top)*. D-APV application (100 μM) blocks CaTs *(bottom)*. (**B**) Quantified ΔG/R
906 signals before and after D-APV application. (**C**) Summary data of D-APV block on glutamate
907 uncaging elicited CaTs (baseline 0.0103 ± 0.0016, D-APV -0.004 ± 0.0024, n = 4 boutons, 3
908 animals; U = 0.0304, Mann-Whitney test, baseline vs D-APV). Data are presented as mean ±
909 s.e.m. * U < 0.05.
910
911 **Figure 7. preNMDARs contribute significantly to BDNF release following repetitive activity.**
912 (**A**) Representative images showing expression of BDNF-pHluorin in the DG and CA3 area
913 (arrows indicate mf axon, arrowheads indicate mf boutons). Control images *(top)*, *Grin1*-cKO
914 images *(bottom)*. (**B**) Representative images of BDNF-pHluorin signal intensity at baseline and
915 after repetitive stimulation of mfs (125 pulses, 25 Hz, x 2). Control images *(left)*, *Grin1*-cKO images
916 *(right*), arrowhead indicates region of interest. (**C**) Time course of BDNF-pHluorin signal intensity
917 measured as ΔF/F (%): control *(black)*, *Grin1*-cKO *(red),* Naïve *(blue)*. (**D**) Quantification of BDNF-
918 pHluorin signal in (C) during the last 100 seconds reveals larger BDNF release in control animals
919 as compared to *Grin1*-cKO (control -18% ± 3%, n = 12 slices, 5 animals; *Grin1*-cKO -8 ± 1%, n =
920 10 slices, 5 animals; *Grin1*-cKO vs. control, p = 0.00648, unpaired *t*-test). Data are presented as
921 mean ± s.e.m. ** p < 0.01.
922
923 **Supplementary Figure 11 related to Figure 7.** preNMDARs contribute significantly to BDNF
924 release following a more physiological pattern of burst-stimulation. (**A**) Representative images of

925 BDNF-pHluorin signal intensity at baseline and after burst stimulation of mfs (5 pulses, 100 Hz, x
926 50, every 0.5 s). Control images *(left)*, *Grin1*-cKO images *(right*), arrowhead indicates region of
927 interest. (**B**) Time course of BDNF-pHluorin signal intensity measured as ΔF/F (%): control *(black)*,
928 *Grin1*-cKO *(red),* Naïve *(blue)*. (**C**) Quantification of BDNF-pHluorin signal in (B) during the last
929 100 seconds reveals larger BDNF release in control animals as compared to *Grin1*-cKO (control
930 -8.9% ± 2%, n = 7 slices, 5 animals; *Grin1*-cKO -3.5 ± 1%, n = 11 slices, 5 animals; *Grin1*-cKO
931 vs. control, p = 0.0305, unpaired *t*-test). Data are presented as mean ± s.e.m. * p < 0.05.
932
933 **Figure 8. preNMDARs contribute to synaptic facilitation of mossy fiber inputs onto mossy**
934 **cells but not onto CA3 inhibitory interneurons.** (**A**) Representative images showing a CA3
935 interneuron and a hilar mossy cell patch-loaded with Alexa 594 (35 μM) for morphological
936 identification in acute rat hippocampal slices. (**B**) AMPAR-EPSCs were recorded from CA3
937 interneurons at V_h= -65 mV and burst-stimulation was elicited by 5 pulses at 25 Hz, see traces
938 *(top)*. Representative experiment *(bottom, left)*, and summary plots *(right)* showing bath-
939 application of MK-801 (50 μM) had no significant effect on depression *(top, right)* or facilitation
940 *(bottom, right)* measured by P5/P1 ratio (baseline 54 ± 12%, MK-801 60 ± 16%, n = 6 cells; MK-
941 801 vs baseline, p = 0.675, Wilcoxon Signed Ranks test; baseline 281 ± 30%, MK-801 318 ± 37%,
942 n = 7 cells; MK-801 vs baseline, p = 0.178, paired *t*-test, 5 animals in each data set). (**C**) AMPAR-
943 ESPCs were recorded at V_h = -70 mV from hilar mossy cells, LFF was induced by stepping
944 stimulation frequency from 0.1 to 1 Hz, see traces *(top)*. Representative experiment *(middle)*,
945 normalized LFF and summary plot *(bottom)* indicating bath-application of MK-801 (50 μM)
946 reduced facilitation (baseline 350 ± 10%, MK-801 225 ± 25%, n = 9 cells, 6 animals; baseline vs
947 MK-801, p = 0.00152, paired *t*-test). DCG-IV (1 μM) was applied at the end of all experiments.
948 Data are presented as mean ± s.e.m. *** p < 0.005.
949
950 **Supplementary Figure 12 related to Figure 8.** Stability experiments for mf-Interneuron and mf-

951 mossy cell short-term plasticity. (**A**) Stable CA3 interneuron burst-induced facilitation of mf-CA3
952 transmission (baseline 273 ± 30%, naïve 294 ± 33%, n = 10 cells, 6 animals; p = 0.298, paired *t*-
953 test, baseline vs naïve). (**B**) Stable low-frequency facilitation (LFF) of AMPAR-EPSCs in hilar
954 mossy cells (baseline 288 ± 51%, naïve 291 ± 29%, n = 7 cells, 6 animals; p = 0.937, paired *t*-
955 test, baseline vs naïve). DCG-IV (1 μM) was applied at the end of all recordings to confirm mf-
956 CA3 transmission. Data are presented as mean ± s.e.m.
957
958
959
960
961
962
963
964
965
966
967
968
969
970
971
972
973
974
975
976

REFERENCES

Abbott, L. F., & Regehr, W. G. (2004). Synaptic computation. *Nature, 431*(7010), 796-803. doi:10.1038/nature03010

Abrahamsson, T., Chou, C. Y. C., Li, S. Y., Mancino, A., Costa, R. P., Brock, J. A., . . . Sjostrom, P. J. (2017). Differential Regulation of Evoked and Spontaneous Release by Presynaptic NMDA Receptors. *Neuron, 96*(4), 839-855 e835. doi:10.1016/j.neuron.2017.09.030

Alle, H., & Geiger, J. R. (2006). Combined analog and action potential coding in hippocampal mossy fibers. *Science, 311*(5765), 1290-1293. doi:10.1126/science.1119055

Amaral, D. G., & Dent, J. A. (1981). Development of the mossy fibers of the dentate gyrus: I. A light and electron microscopic study of the mossy fibers and their expansions. *J Comp Neurol, 195*(1), 51-86. doi:10.1002/cne.901950106

Amaral, D. G., Scharfman, H. E., & Lavenex, P. (2007). The dentate gyrus: fundamental neuroanatomical organization (dentate gyrus for dummies). *Prog Brain Res, 163*, 3-22. doi:S0079-6123(07)63001-5 [pii]
10.1016/S0079-6123(07)63001-5

Banerjee, A., Larsen, R. S., Philpot, B. D., & Paulsen, O. (2016). Roles of Presynaptic NMDA Receptors in Neurotransmission and Plasticity. *Trends Neurosci, 39*(1), 26-39. doi:10.1016/j.tins.2015.11.001

Berg, L. K., Larsson, M., Morland, C., & Gundersen, V. (2013). Pre- and postsynaptic localization of NMDA receptor subunits at hippocampal mossy fibre synapses. *Neuroscience, 230*, 139-150. doi:10.1016/j.neuroscience.2012.10.061

Berretta, N., & Jones, R. S. (1996). Tonic facilitation of glutamate release by presynaptic N-methyl-D-aspartate autoreceptors in the entorhinal cortex. *Neuroscience, 75*(2), 339-344. doi:10.1016/0306-4522(96)00301-6

Bischofberger, J., Engel, D., Frotscher, M., & Jonas, P. (2006). Timing and efficacy of transmitter release at mossy fiber synapses in the hippocampal network. *Pflugers Arch, 453*(3), 361-372. doi:10.1007/s00424-006-0093-2

Bouvier, G., Bidoret, C., Casado, M., & Paoletti, P. (2015). Presynaptic NMDA receptors: Roles and rules. *Neuroscience, 311*, 322-340. doi:10.1016/j.neuroscience.2015.10.033

Bouvier, G., Higgins, D., Spolidoro, M., Carrel, D., Mathieu, B., Lena, C., . . . Casado, M. (2016). Burst-Dependent Bidirectional Plasticity in the Cerebellum Is Driven by Presynaptic NMDA Receptors. *Cell Rep, 15*(1), 104-116. doi:10.1016/j.celrep.2016.03.004

Bouvier, G., Larsen, R. S., Rodriguez-Moreno, A., Paulsen, O., & Sjostrom, P. J. (2018). Towards resolving the presynaptic NMDA receptor debate. *Curr Opin Neurobiol, 51*, 1-7. doi:10.1016/j.conb.2017.12.020

Buchanan, K. A., Blackman, A. V., Moreau, A. W., Elgar, D., Costa, R. P., Lalanne, T., . . . Sjostrom, P. J. (2012). Target-specific expression of presynaptic NMDA receptors in neocortical microcircuits. *Neuron, 75*(3), 451-466. doi:10.1016/j.neuron.2012.06.017

Burke, K. J., Jr., & Bender, K. J. (2019). Modulation of Ion Channels in the Axon: Mechanisms and Function. *Front Cell Neurosci, 13*, 221. doi:10.3389/fncel.2019.00221

Carter, B. C., & Jahr, C. E. (2016). Postsynaptic, not presynaptic NMDA receptors are required for spike-timing-dependent LTD induction. *Nat Neurosci, 19*(9), 1218-1224. doi:10.1038/nn.4343

Castillo, P. E. (2012). Presynaptic LTP and LTD of excitatory and inhibitory synapses. *Cold Spring Harb Perspect Biol, 4*(2). doi:10.1101/cshperspect.a005728

Castillo, P. E., Malenka, R. C., & Nicoll, R. A. (1997). Kainate receptors mediate a slow postsynaptic current in hippocampal CA3 neurons. *Nature, 388*(6638), 182-186. doi:10.1038/40645

Chamberland, S., Timofeeva, Y., Evstratova, A., Volynski, K., & Toth, K. (2018). Action potential counting at giant mossy fiber terminals gates information transfer in the hippocampus.

Proc Natl Acad Sci U S A, 115(28), 7434-7439. doi:10.1073/pnas.1720659115
Chen, W., Walwyn, W., Ennes, H. S., Kim, H., McRoberts, J. A., & Marvizon, J. C. (2014). BDNF released during neuropathic pain potentiates NMDA receptors in primary afferent terminals. *Eur J Neurosci, 39*(9), 1439-1454. doi:10.1111/ejn.12516
Chen, Y., Chen, S. R., Chen, H., Zhang, J., & Pan, H. L. (2019). Increased alpha2delta-1-NMDA receptor coupling potentiates glutamatergic input to spinal dorsal horn neurons in chemotherapy-induced neuropathic pain. *J Neurochem, 148*(2), 252-274. doi:10.1111/jnc.14627
Christie, J. M., & Jahr, C. E. (2008). Dendritic NMDA receptors activate axonal calcium channels. *Neuron, 60*(2), 298-307. doi:10.1016/j.neuron.2008.08.028
Christie, J. M., & Jahr, C. E. (2009). Selective expression of ligand-gated ion channels in L5 pyramidal cell axons. *J Neurosci, 29*(37), 11441-11450. doi:10.1523/JNEUROSCI.2387-09.2009
Conner, J. M., Lauterborn, J. C., Yan, Q., Gall, C. M., & Varon, S. (1997). Distribution of brain-derived neurotrophic factor (BDNF) protein and mRNA in the normal adult rat CNS: evidence for anterograde axonal transport. *J Neurosci, 17*(7), 2295-2313. Retrieved from https://www.ncbi.nlm.nih.gov/pubmed/9065491
Corlew, R., Brasier, D. J., Feldman, D. E., & Philpot, B. D. (2008). Presynaptic NMDA receptors: newly appreciated roles in cortical synaptic function and plasticity. *Neuroscientist, 14*(6), 609-625. doi:10.1177/1073858408322675
Corlew, R., Wang, Y., Ghermazien, H., Erisir, A., & Philpot, B. D. (2007). Developmental switch in the contribution of presynaptic and postsynaptic NMDA receptors to long-term depression. *J Neurosci, 27*(37), 9835-9845. doi:10.1523/JNEUROSCI.5494-06.2007
Cull-Candy, S., Brickley, S., & Farrant, M. (2001). NMDA receptor subunits: diversity, development and disease. *Curr Opin Neurobiol, 11*(3), 327-335. Retrieved from https://www.ncbi.nlm.nih.gov/pubmed/11399431
Diamantaki, M., Frey, M., Berens, P., Preston-Ferrer, P., & Burgalossi, A. (2016). Sparse activity of identified dentate granule cells during spatial exploration. *Elife, 5*. doi:10.7554/eLife.20252
Dore, K., Aow, J., & Malinow, R. (2016). The Emergence of NMDA Receptor Metabotropic Function: Insights from Imaging. *Front Synaptic Neurosci, 8*, 20. doi:10.3389/fnsyn.2016.00020
Duguid, I. C. (2013). Presynaptic NMDA receptors: are they dendritic receptors in disguise? *Brain Res Bull, 93*, 4-9. doi:10.1016/j.brainresbull.2012.12.004
Duguid, I. C., & Smart, T. G. (2009). Presynaptic NMDA Receptors. In A. M. Van Dongen (Ed.), *Biology of the NMDA Receptor*. Boca Raton (FL).
Engelman, H. S., & MacDermott, A. B. (2004). Presynaptic ionotropic receptors and control of transmitter release. *Nat Rev Neurosci, 5*(2), 135-145. doi:10.1038/nrn1297
Evstratova, A., & Toth, K. (2014). Information processing and synaptic plasticity at hippocampal mossy fiber terminals. *Front Cell Neurosci, 8*, 28. doi:10.3389/fncel.2014.00028
Fujisawa, S., & Aoki, C. (2003). In vivo blockade of N-methyl-D-aspartate receptors induces rapid trafficking of NR2B subunits away from synapses and out of spines and terminals in adult cortex. *Neuroscience, 121*(1), 51-63. doi:10.1016/s0306-4522(03)00341-5
Gill, I., Droubi, S., Giovedi, S., Fedder, K. N., Bury, L. A., Bosco, F., . . . Sabo, S. L. (2015). Presynaptic NMDA receptors - dynamics and distribution in developing axons in vitro and in vivo. *J Cell Sci, 128*(4), 768-780. doi:10.1242/jcs.162362
GoodSmith, D., Chen, X., Wang, C., Kim, S. H., Song, H., Burgalossi, A., . . . Knierim, J. J. (2017). Spatial Representations of Granule Cells and Mossy Cells of the Dentate Gyrus. *Neuron, 93*(3), 677-690 e675. doi:10.1016/j.neuron.2016.12.026
Hagena, H., & Manahan-Vaughan, D. (2010). Frequency facilitation at mossy fiber-CA3 synapses of freely behaving rats contributes to the induction of persistent LTD via an adenosine-A1

1079 receptor-regulated mechanism. *Cereb Cortex, 20*(5), 1121-1130.
1080 doi:10.1093/cercor/bhp184
1081 Henze, D. A., Urban, N. N., & Barrionuevo, G. (2000). The multifarious hippocampal mossy fiber
1082 pathway: a review. *Neuroscience, 98*(3), 407-427. Retrieved from
1083 https://www.ncbi.nlm.nih.gov/pubmed/10869836
1084 Henze, D. A., Wittner, L., & Buzsaki, G. (2002). Single granule cells reliably discharge targets in
1085 the hippocampal CA3 network in vivo. *Nat Neurosci, 5*(8), 790-795. doi:10.1038/nn887
1086 Jackman, S. L., & Regehr, W. G. (2017). The Mechanisms and Functions of Synaptic Facilitation.
1087 *Neuron, 94*(3), 447-464. doi:10.1016/j.neuron.2017.02.047
1088 Jourdain, P., Bergersen, L. H., Bhaukaurally, K., Bezzi, P., Santello, M., Domercq, M., . . . Volterra,
1089 A. (2007). Glutamate exocytosis from astrocytes controls synaptic strength. *Nat Neurosci,*
1090 *10*(3), 331-339. doi:10.1038/nn1849
1091 Kamiya, H., Shinozaki, H., & Yamamoto, C. (1996). Activation of metabotropic glutamate receptor
1092 type 2/3 suppresses transmission at rat hippocampal mossy fibre synapses. *J Physiol,*
1093 *493 (Pt 2)*, 447-455. doi:10.1113/jphysiol.1996.sp021395
1094 Klug, A., Borst, J. G., Carlson, B. A., Kopp-Scheinpflug, C., Klyachko, V. A., & Xu-Friedman, M.
1095 A. (2012). How do short-term changes at synapses fine-tune information processing? *J*
1096 *Neurosci, 32*(41), 14058-14063. doi:10.1523/JNEUROSCI.3348-12.2012
1097 Kunz, P. A., Roberts, A. C., & Philpot, B. D. (2013). Presynaptic NMDA receptor mechanisms for
1098 enhancing spontaneous neurotransmitter release. *J Neurosci, 33*(18), 7762-7769.
1099 doi:10.1523/JNEUROSCI.2482-12.2013
1100 Kwon, H. B., & Castillo, P. E. (2008). Role of glutamate autoreceptors at hippocampal mossy fiber
1101 synapses. *Neuron, 60*(6), 1082-1094. doi:10.1016/j.neuron.2008.10.045
1102 Larsen, R. S., Corlew, R. J., Henson, M. A., Roberts, A. C., Mishina, M., Watanabe, M., . . . Philpot,
1103 B. D. (2011). NR3A-containing NMDARs promote neurotransmitter release and spike
1104 timing-dependent plasticity. *Nat Neurosci, 14*(3), 338-344. doi:10.1038/nn.2750
1105 Larsen, R. S., & Sjostrom, P. J. (2015). Synapse-type-specific plasticity in local circuits. *Curr Opin*
1106 *Neurobiol, 35*, 127-135. doi:10.1016/j.conb.2015.08.001
1107 Larsen, R. S., Smith, I. T., Miriyala, J., Han, J. E., Corlew, R. J., Smith, S. L., & Philpot, B. D.
1108 (2014). Synapse-specific control of experience-dependent plasticity by presynaptic NMDA
1109 receptors. *Neuron, 83*(4), 879-893. doi:10.1016/j.neuron.2014.07.039
1110 Lau, C. G., & Zukin, R. S. (2007). NMDA receptor trafficking in synaptic plasticity and
1111 neuropsychiatric disorders. *Nat Rev Neurosci, 8*(6), 413-426. doi:10.1038/nrn2153
1112 Lawrence, J. J., & McBain, C. J. (2003). Interneuron diversity series: containing the detonation--
1113 feedforward inhibition in the CA3 hippocampus. *Trends Neurosci, 26*(11), 631-640.
1114 doi:10.1016/j.tins.2003.09.007
1115 Liang, Y., Yuan, L. L., Johnston, D., & Gray, R. (2002). Calcium signaling at single mossy fiber
1116 presynaptic terminals in the rat hippocampus. *J Neurophysiol, 87*(2), 1132-1137.
1117 doi:10.1152/jn.00661.2001
1118 Lujan, R., Nusser, Z., Roberts, J. D., Shigemoto, R., & Somogyi, P. (1996). Perisynaptic location
1119 of metabotropic glutamate receptors mGluR1 and mGluR5 on dendrites and dendritic
1120 spines in the rat hippocampus. *Eur J Neurosci, 8*(7), 1488-1500. Retrieved from
1121 https://www.ncbi.nlm.nih.gov/pubmed/8758956
1122 Lysetskiy, M., Foldy, C., & Soltesz, I. (2005). Long- and short-term plasticity at mossy fiber
1123 synapses on mossy cells in the rat dentate gyrus. *Hippocampus, 15*(6), 691-696.
1124 doi:10.1002/hipo.20096
1125 Madara, J. C., & Levine, E. S. (2008). Presynaptic and postsynaptic NMDA receptors mediate
1126 distinct effects of brain-derived neurotrophic factor on synaptic transmission. *J*
1127 *Neurophysiol, 100*(6), 3175-3184. doi:10.1152/jn.90880.2008
1128 Mameli, M., Carta, M., Partridge, L. D., & Valenzuela, C. F. (2005). Neurosteroid-induced plasticity
1129 of immature synapses via retrograde modulation of presynaptic NMDA receptors. *J*

Neurosci, 25(9), 2285-2294. doi:10.1523/JNEUROSCI.3877-04.2005
Martin, D., Bustos, G. A., Bowe, M. A., Bray, S. D., & Nadler, J. V. (1991). Autoreceptor regulation of glutamate and aspartate release from slices of the hippocampal CA1 area. *J Neurochem, 56*(5), 1647-1655. doi:10.1111/j.1471-4159.1991.tb02063.x
McGuinness, L., Taylor, C., Taylor, R. D., Yau, C., Langenhan, T., Hart, M. L., . . . Emptage, N. J. (2010). Presynaptic NMDARs in the hippocampus facilitate transmitter release at theta frequency. *Neuron, 68*(6), 1109-1127. doi:10.1016/j.neuron.2010.11.023
McHugh, T. J., Jones, M. W., Quinn, J. J., Balthasar, N., Coppari, R., Elmquist, J. K., . . . Tonegawa, S. (2007). Dentate gyrus NMDA receptors mediate rapid pattern separation in the hippocampal network. *Science, 317*(5834), 94-99. doi:10.1126/science.1140263
McNamara, J. O., & Scharfman, H. E. (2012). Temporal Lobe Epilepsy and the BDNF Receptor, TrkB. In th, J. L. Noebels, M. Avoli, M. A. Rogawski, R. W. Olsen, & A. V. Delgado-Escueta (Eds.), *Jasper's Basic Mechanisms of the Epilepsies*. Bethesda (MD).
Miller, R. J. (1998). Presynaptic receptors. *Annu Rev Pharmacol Toxicol, 38*, 201-227. doi:10.1146/annurev.pharmtox.38.1.201
Nicoll, R. A., & Schmitz, D. (2005). Synaptic plasticity at hippocampal mossy fibre synapses. *Nat Rev Neurosci, 6*(11), 863-876. doi:10.1038/nrn1786
Nusser, Z., Lujan, R., Laube, G., Roberts, J. D., Molnar, E., & Somogyi, P. (1998). Cell type and pathway dependence of synaptic AMPA receptor number and variability in the hippocampus. *Neuron, 21*(3), 545-559. Retrieved from https://www.ncbi.nlm.nih.gov/pubmed/9768841
Paoletti, P., Bellone, C., & Zhou, Q. (2013). NMDA receptor subunit diversity: impact on receptor properties, synaptic plasticity and disease. *Nat Rev Neurosci, 14*(6), 383-400. doi:10.1038/nrn3504
Park, H., Popescu, A., & Poo, M. M. (2014). Essential role of presynaptic NMDA receptors in activity-dependent BDNF secretion and corticostriatal LTP. *Neuron, 84*(5), 1009-1022. doi:10.1016/j.neuron.2014.10.045
Pernia-Andrade, A. J., & Jonas, P. (2014). Theta-gamma-modulated synaptic currents in hippocampal granule cells in vivo define a mechanism for network oscillations. *Neuron, 81*(1), 140-152. doi:10.1016/j.neuron.2013.09.046
Petralia, R. S., Yokotani, N., & Wenthold, R. J. (1994). Light and electron microscope distribution of the NMDA receptor subunit NMDAR1 in the rat nervous system using a selective anti-peptide antibody. *J Neurosci, 14*(2), 667-696. Retrieved from https://www.ncbi.nlm.nih.gov/pubmed/8301357
Pickel, V. M., Colago, E. E., Mania, I., Molosh, A. I., & Rainnie, D. G. (2006). Dopamine D1 receptors co-distribute with N-methyl-D-aspartic acid type-1 subunits and modulate synaptically-evoked N-methyl-D-aspartic acid currents in rat basolateral amygdala. *Neuroscience, 142*(3), 671-690. doi:10.1016/j.neuroscience.2006.06.059
Pinheiro, P. S., & Mulle, C. (2008). Presynaptic glutamate receptors: physiological functions and mechanisms of action. *Nat Rev Neurosci, 9*(6), 423-436. doi:10.1038/nrn2379
Rebola, N., Carta, M., & Mulle, C. (2017). Operation and plasticity of hippocampal CA3 circuits: implications for memory encoding. *Nat Rev Neurosci, 18*(4), 208-220. doi:10.1038/nrn.2017.10
Rogers, M., & Dani, J. A. (1995). Comparison of quantitative calcium flux through NMDA, ATP, and ACh receptor channels. *Biophys J, 68*(2), 501-506. doi:10.1016/S0006-3495(95)80211-0
Rossi, B., Ogden, D., Llano, I., Tan, Y. P., Marty, A., & Collin, T. (2012). Current and calcium responses to local activation of axonal NMDA receptors in developing cerebellar molecular layer interneurons. *PLoS One, 7*(6), e39983. doi:10.1371/journal.pone.0039983
Salin, P. A., Scanziani, M., Malenka, R. C., & Nicoll, R. A. (1996). Distinct short-term plasticity at two excitatory synapses in the hippocampus. *Proc Natl Acad Sci U S A, 93*(23), 13304-

13309. Retrieved from https://www.ncbi.nlm.nih.gov/pubmed/8917586
Sanz-Clemente, A., Nicoll, R. A., & Roche, K. W. (2013). Diversity in NMDA receptor composition: many regulators, many consequences. *Neuroscientist, 19*(1), 62-75. doi:10.1177/1073858411435129
Savtchouk, I., Di Castro, M. A., Ali, R., Stubbe, H., Lujan, R., & Volterra, A. (2019). Circuit-specific control of the medial entorhinal inputs to the dentate gyrus by atypical presynaptic NMDARs activated by astrocytes. *Proc Natl Acad Sci U S A, 116*(27), 13602-13610. doi:10.1073/pnas.1816013116
Schicker, K. W., Dorostkar, M. M., & Boehm, S. (2008). Modulation of transmitter release via presynaptic ligand-gated ion channels. *Curr Mol Pharmacol, 1*(2), 106-129. doi:10.2174/1874467210801020106
Schildt, S., Endres, T., Lessmann, V., & Edelmann, E. (2013). Acute and chronic interference with BDNF/TrkB-signaling impair LTP selectively at mossy fiber synapses in the CA3 region of mouse hippocampus. *Neuropharmacology, 71*, 247-254. doi:10.1016/j.neuropharm.2013.03.041
Senzai, Y., & Buzsaki, G. (2017). Physiological Properties and Behavioral Correlates of Hippocampal Granule Cells and Mossy Cells. *Neuron, 93*(3), 691-704 e695. doi:10.1016/j.neuron.2016.12.011
Siegel, S. J., Brose, N., Janssen, W. G., Gasic, G. P., Jahn, R., Heinemann, S. F., & Morrison, J. H. (1994). Regional, cellular, and ultrastructural distribution of N-methyl-D-aspartate receptor subunit 1 in monkey hippocampus. *Proc Natl Acad Sci U S A, 91*(2), 564-568. Retrieved from https://www.ncbi.nlm.nih.gov/pubmed/8290563
Takumi, Y., Ramirez-Leon, V., Laake, P., Rinvik, E., & Ottersen, O. P. (1999). Different modes of expression of AMPA and NMDA receptors in hippocampal synapses. *Nat Neurosci, 2*(7), 618-624. doi:10.1038/10172
Toni, N., & Schinder, A. F. (2015). Maturation and Functional Integration of New Granule Cells into the Adult Hippocampus. *Cold Spring Harb Perspect Biol, 8*(1), a018903. doi:10.1101/cshperspect.a018903
Toth, K., Suares, G., Lawrence, J. J., Philips-Tansey, E., & McBain, C. J. (2000). Differential mechanisms of transmission at three types of mossy fiber synapse. *J Neurosci, 20*(22), 8279-8289. Retrieved from https://www.ncbi.nlm.nih.gov/pubmed/11069934
Traynelis, S. F., Wollmuth, L. P., McBain, C. J., Menniti, F. S., Vance, K. M., Ogden, K. K., . . . Dingledine, R. (2010). Glutamate receptor ion channels: structure, regulation, and function. *Pharmacol Rev, 62*(3), 405-496. doi:10.1124/pr.109.002451
Vandael, D., Borges-Merjane, C., Zhang, X., & Jonas, P. (2020). Short-Term Plasticity at Hippocampal Mossy Fiber Synapses Is Induced by Natural Activity Patterns and Associated with Vesicle Pool Engram Formation. *Neuron, 107*(3), 509-521 e507. doi:10.1016/j.neuron.2020.05.013
Vyleta, N. P., Borges-Merjane, C., & Jonas, P. (2016). Plasticity-dependent, full detonation at hippocampal mossy fiber-CA3 pyramidal neuron synapses. *Elife, 5*. doi:10.7554/eLife.17977
Wang, P. Y., Petralia, R. S., Wang, Y. X., Wenthold, R. J., & Brenowitz, S. D. (2011). Functional NMDA receptors at axonal growth cones of young hippocampal neurons. *J Neurosci, 31*(25), 9289-9297. doi:10.1523/JNEUROSCI.5639-10.2011
Watanabe, M., Fukaya, M., Sakimura, K., Manabe, T., Mishina, M., & Inoue, Y. (1998). Selective scarcity of NMDA receptor channel subunits in the stratum lucidum (mossy fibre-recipient layer) of the mouse hippocampal CA3 subfield. *Eur J Neurosci, 10*(2), 478-487. Retrieved from https://www.ncbi.nlm.nih.gov/pubmed/9749710
Wong, H. H., Rannio, S., Jones, V., Thomazeau, A., & Sjostrom, P. J. (2020). NMDA receptors in axons: there's no coincidence. *J Physiol*. doi:10.1113/JP280059
Woodhall, G., Evans, D. I., Cunningham, M. O., & Jones, R. S. (2001). NR2B-containing NMDA

autoreceptors at synapses on entorhinal cortical neurons. *J Neurophysiol, 86*(4), 1644-1651. doi:10.1152/jn.2001.86.4.1644

Yan, Q., Rosenfeld, R. D., Matheson, C. R., Hawkins, N., Lopez, O. T., Bennett, L., & Welcher, A. A. (1997). Expression of brain-derived neurotrophic factor protein in the adult rat central nervous system. *Neuroscience, 78*(2), 431-448. Retrieved from https://www.ncbi.nlm.nih.gov/pubmed/9145800

Yang, J., Woodhall, G. L., & Jones, R. S. (2006). Tonic facilitation of glutamate release by presynaptic NR2B-containing NMDA receptors is increased in the entorhinal cortex of chronically epileptic rats. *J Neurosci, 26*(2), 406-410. doi:10.1523/JNEUROSCI.4413-05.2006

Zeng, J., Thomson, L. M., Aicher, S. A., & Terman, G. W. (2006). Primary afferent NMDA receptors increase dorsal horn excitation and mediate opiate tolerance in neonatal rats. *J Neurosci, 26*(46), 12033-12042. doi:10.1523/JNEUROSCI.2530-06.2006

Zucca, S., Griguoli, M., Malezieux, M., Grosjean, N., Carta, M., & Mulle, C. (2017). Control of Spike Transfer at Hippocampal Mossy Fiber Synapses In Vivo by GABAA and GABAB Receptor-Mediated Inhibition. *J Neurosci, 37*(3), 587-598. doi:10.1523/JNEUROSCI.2057-16.2016

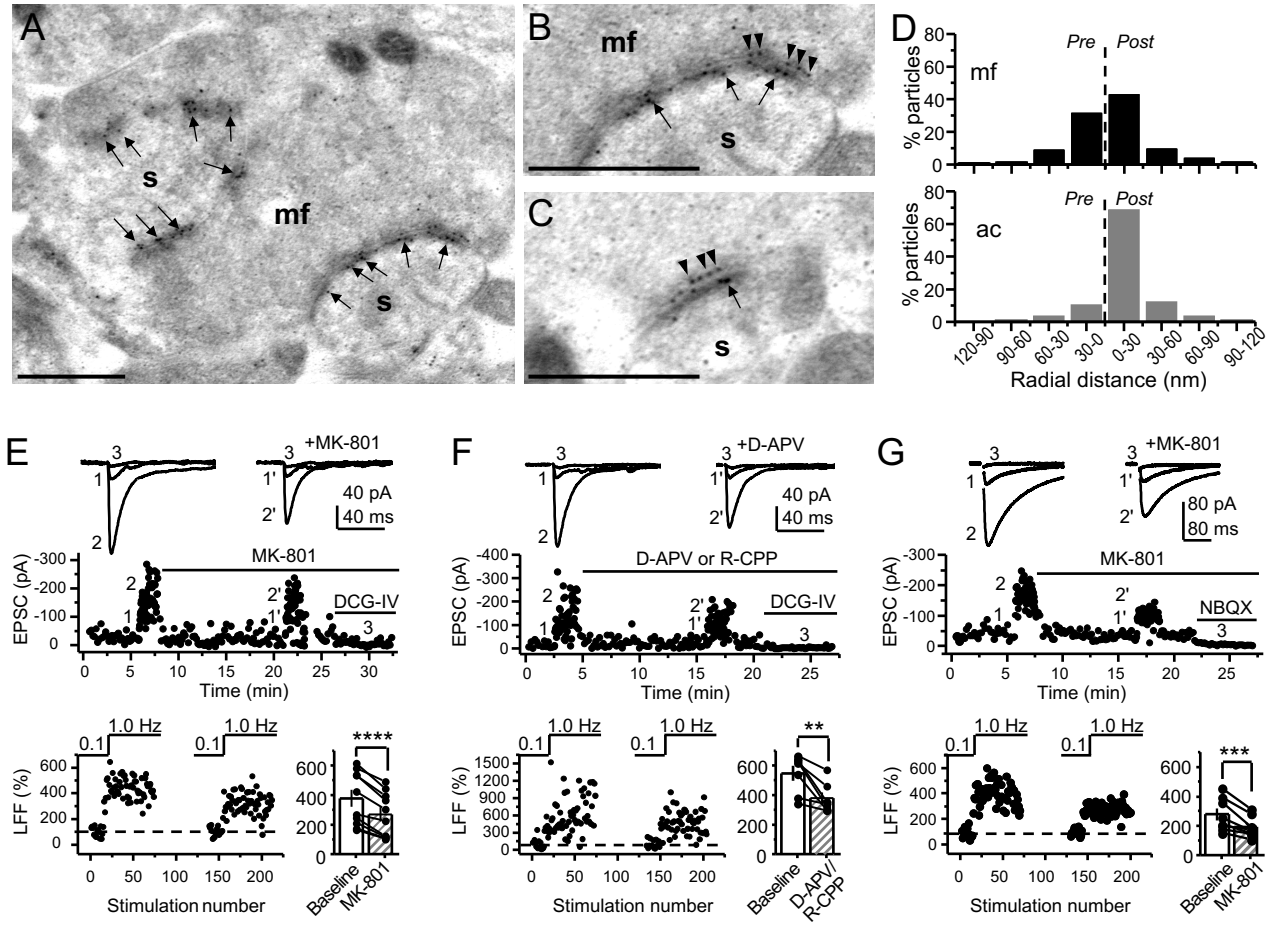

Figure 1. Anatomical and functional evidence for preNMDARs at mossy fiber synapses.

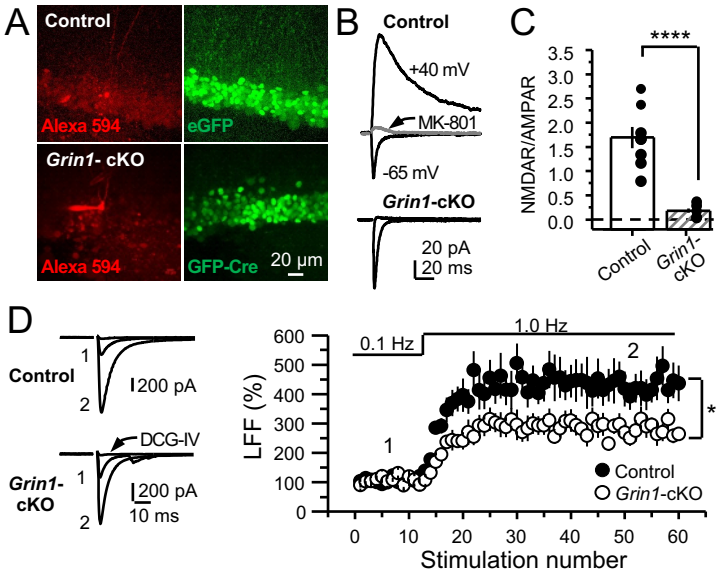

Figure 2. GluN1 deletion from granule cells reduces mf-CA3 facilitation.

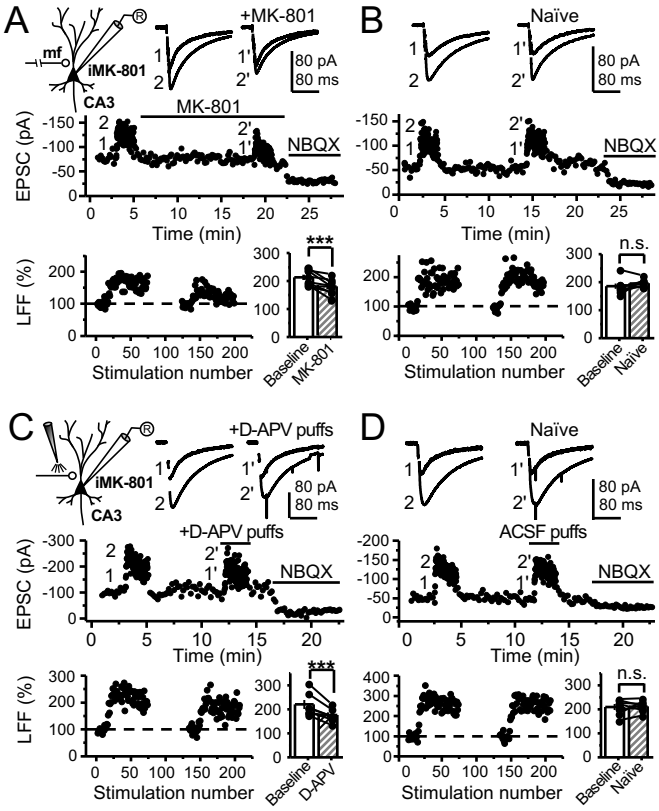

Figure 3. Reduced facilitation by NMDAR antagonism is independent of the GC somatodendritic compartment.

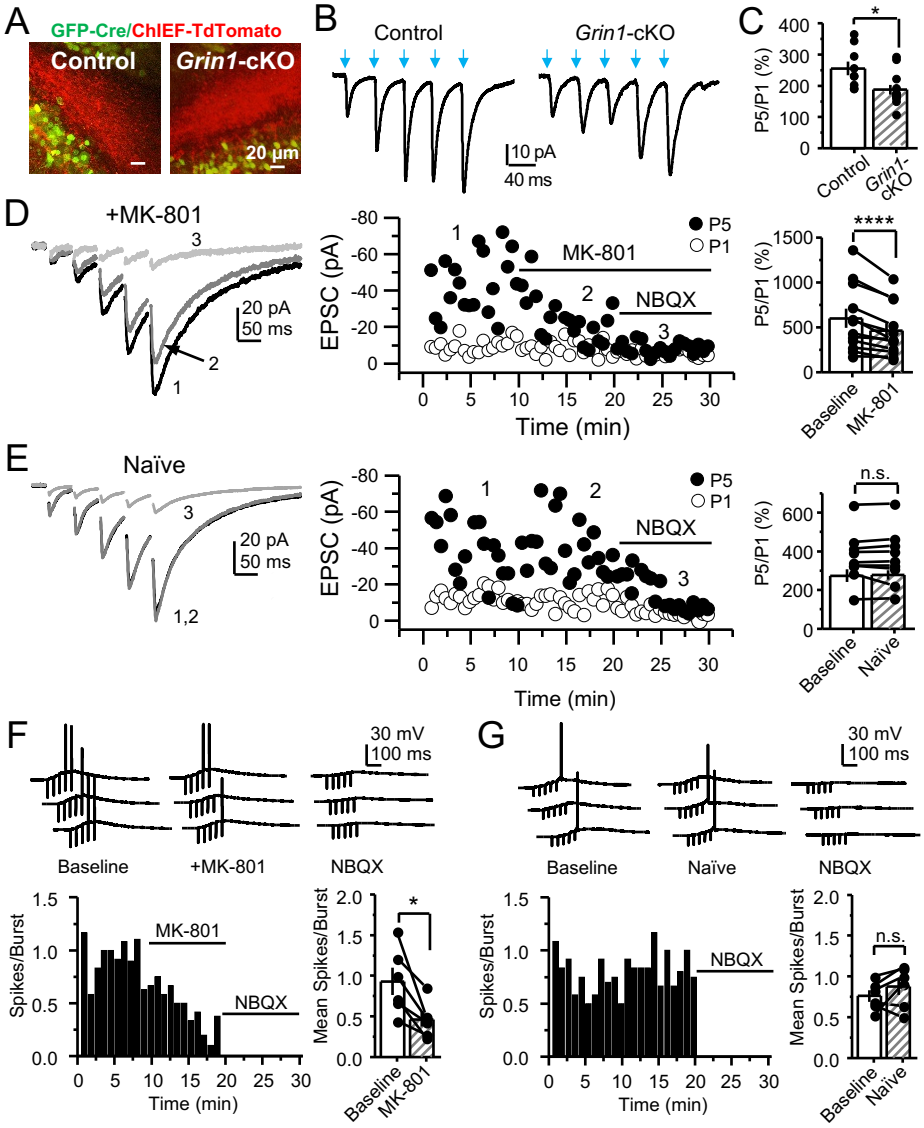

Figure 4. PreNMDARs contribute significantly to burst-induced facilitation and spike transfer.

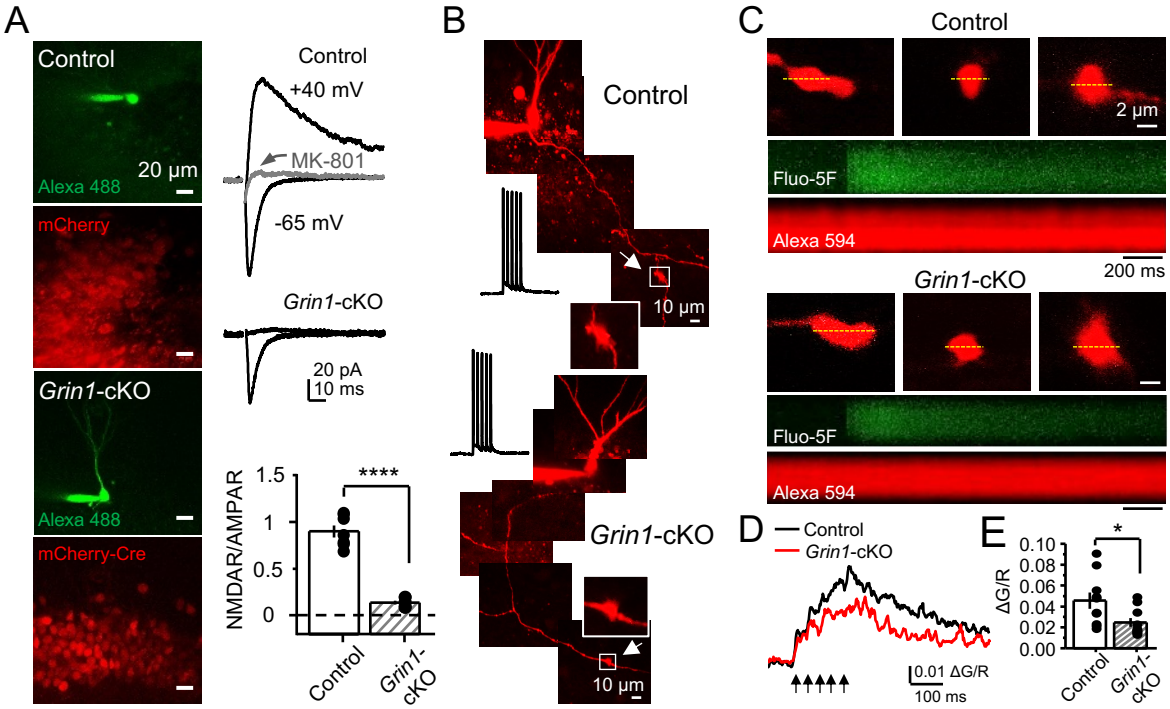

Figure 5. preNMDARs contribute to presynaptic Ca^{2+} rise.

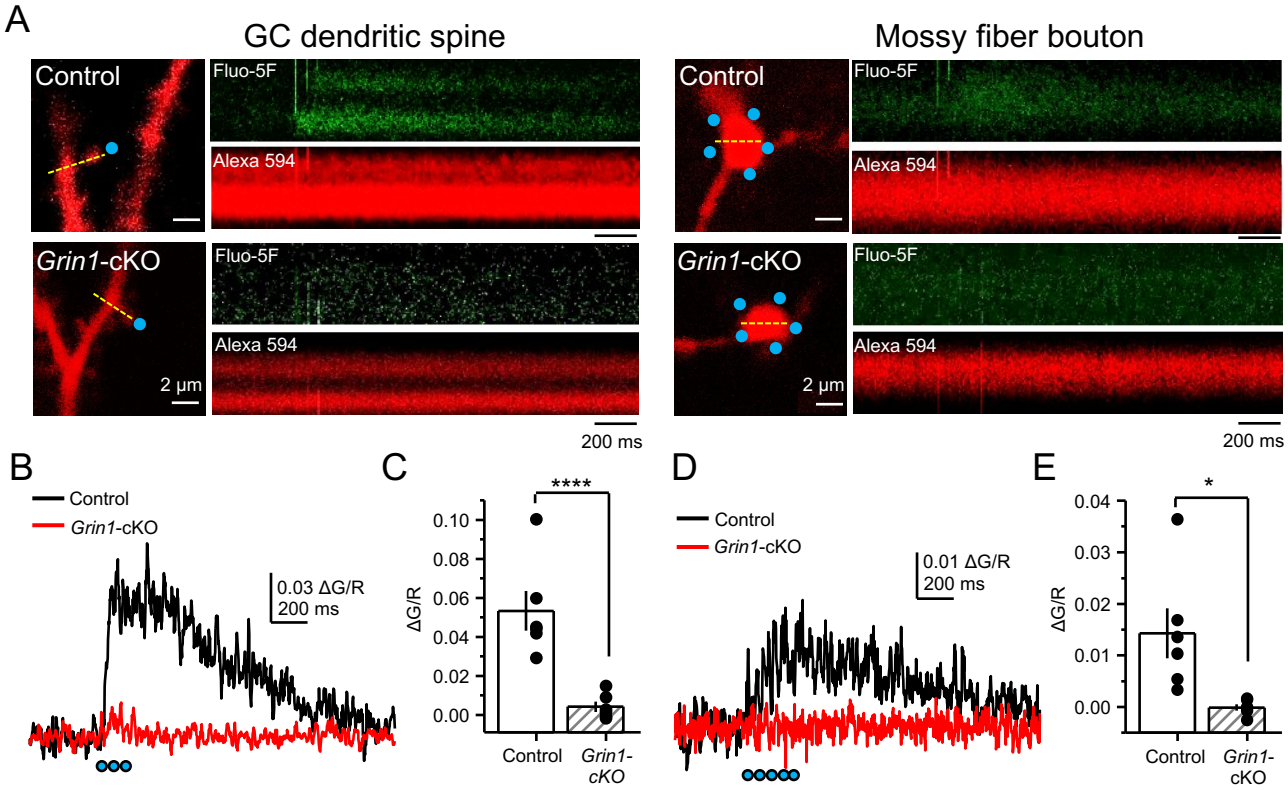

Figure 6. Uncaging glutamate induces Ca^{2+} rise mossy fiber boutons.

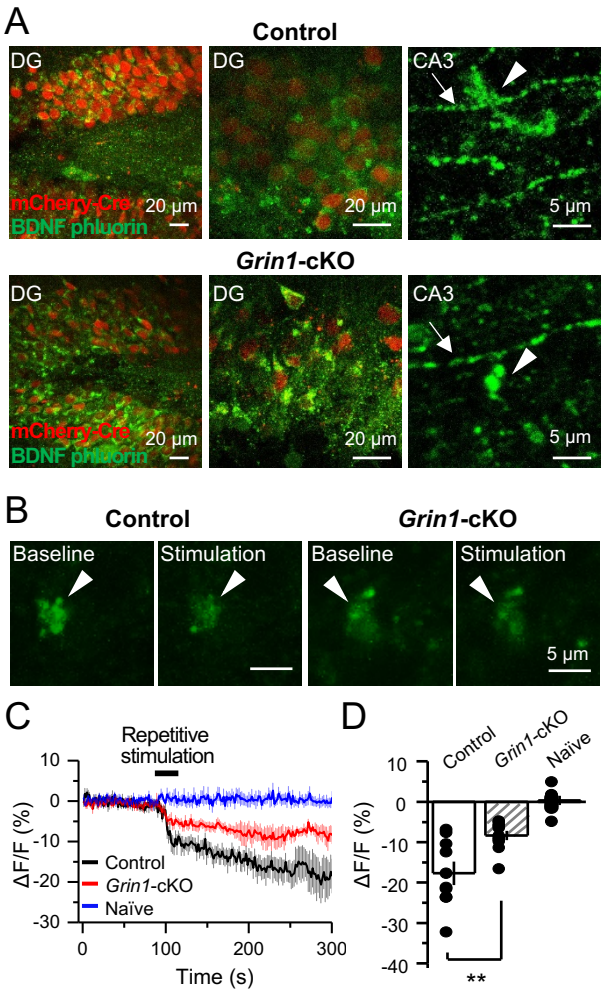

Figure 7. preNMDARs contribute significantly to BDNF release following repetitive activity.

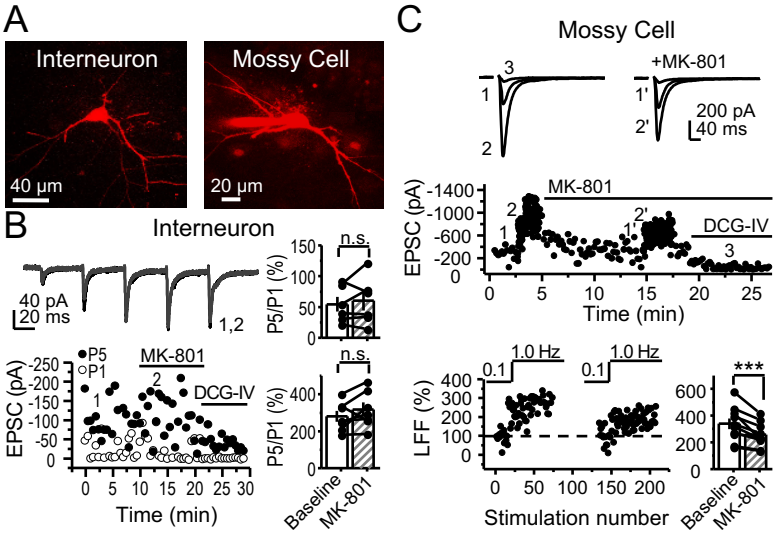

Figure 8. preNMDARs contribute to synaptic facilitation of mossy fiber inputs onto mossy cells but not onto CA3 inhibitory interneurons.

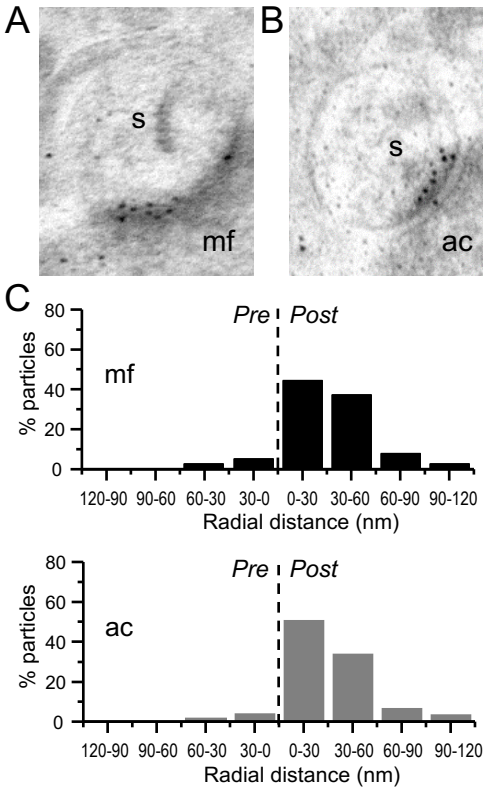

Supplementary Figure 1 related to Figure 1.

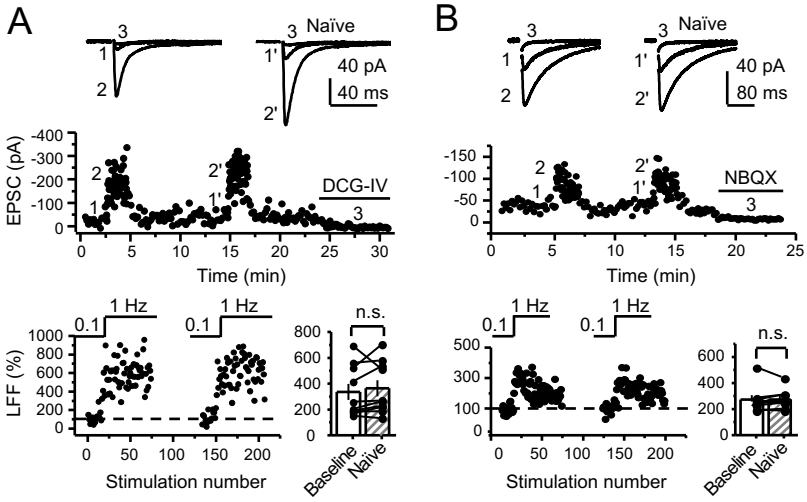

Supplementary Figure 2 related to Figure 1.

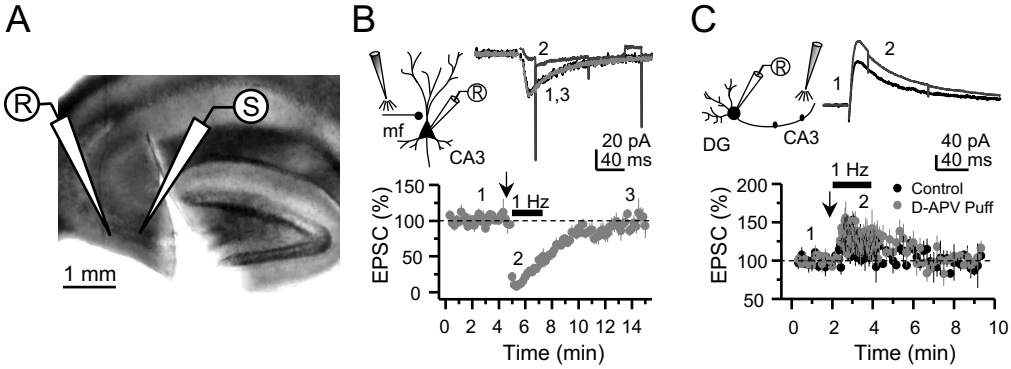

Supplementary Figure 3 related to Figure 3.

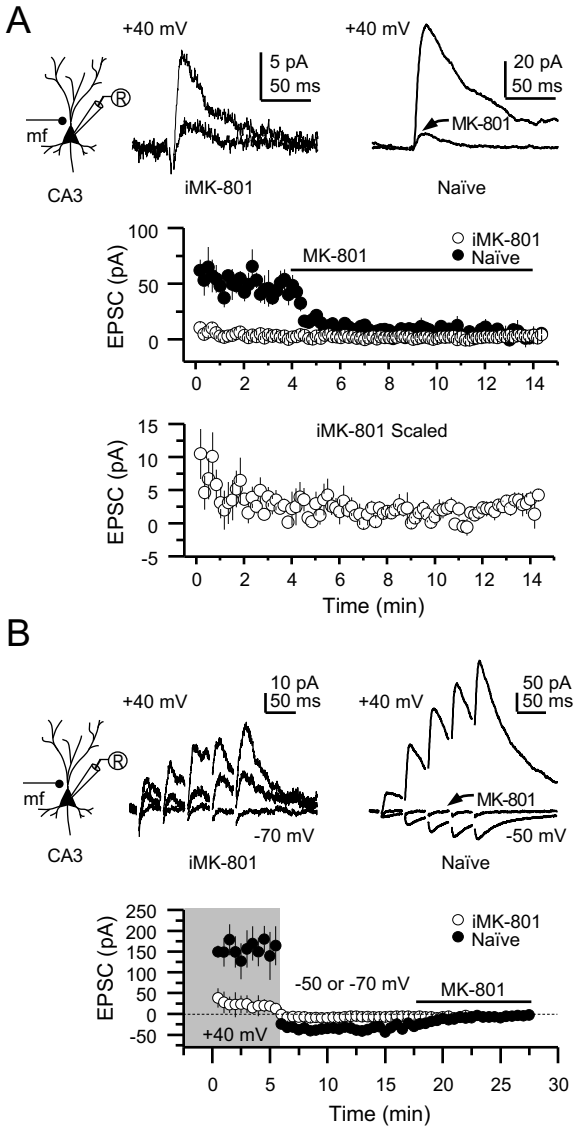

Supplementary Figure 4 related to Figures 1 & 4

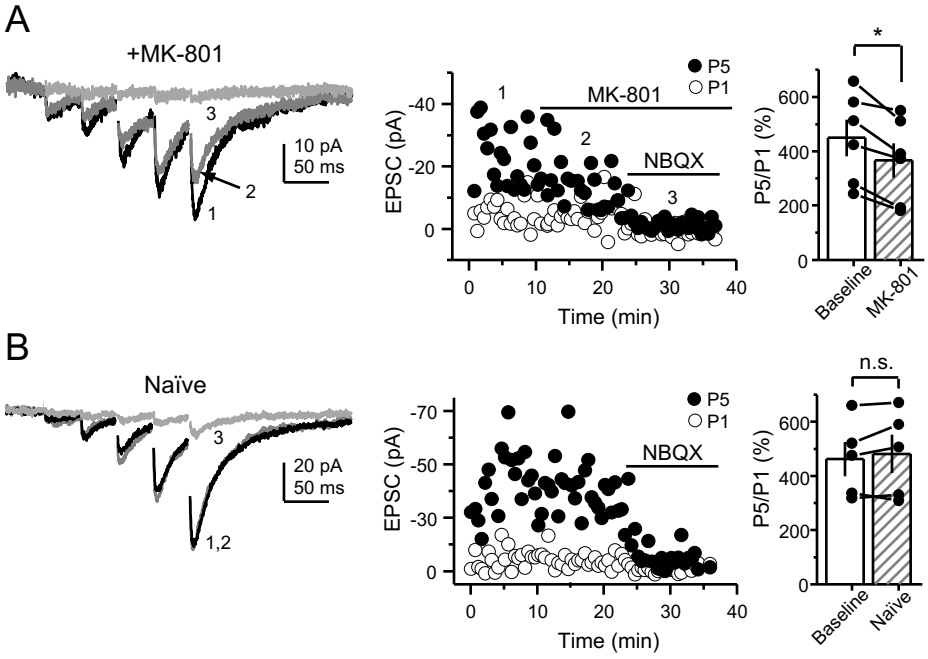

Supplementary Figure 5 related to Figure 4.

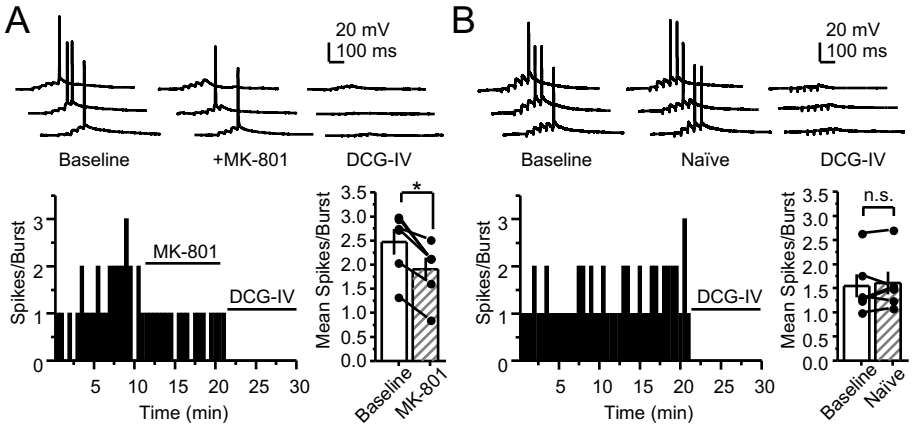

Supplementary Figure 6 related to Figure 4.

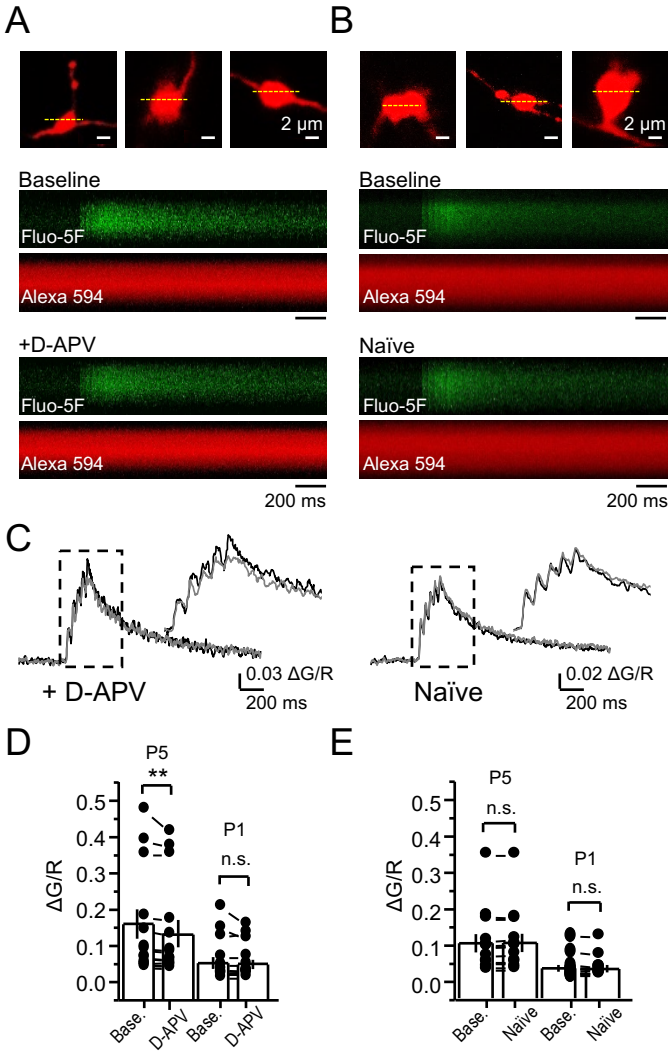

Supplementary Figure 7 related to Figure 5.

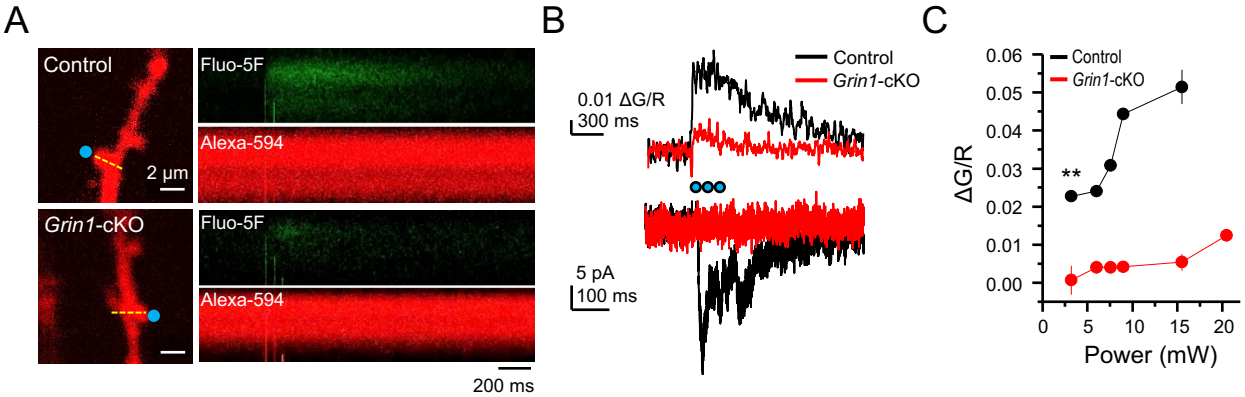

Supplementary Figure 8 related to Figure 6.

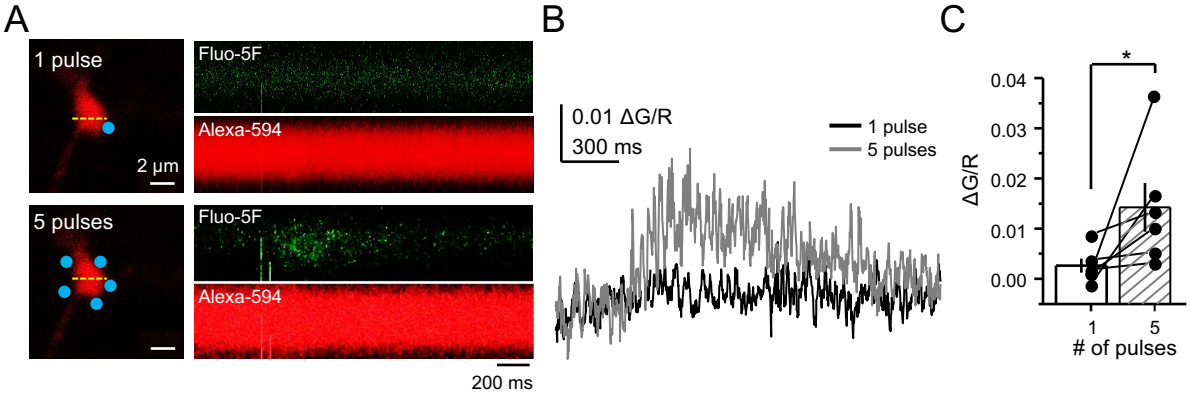

Supplementary Figure 9 related to Figure 6.

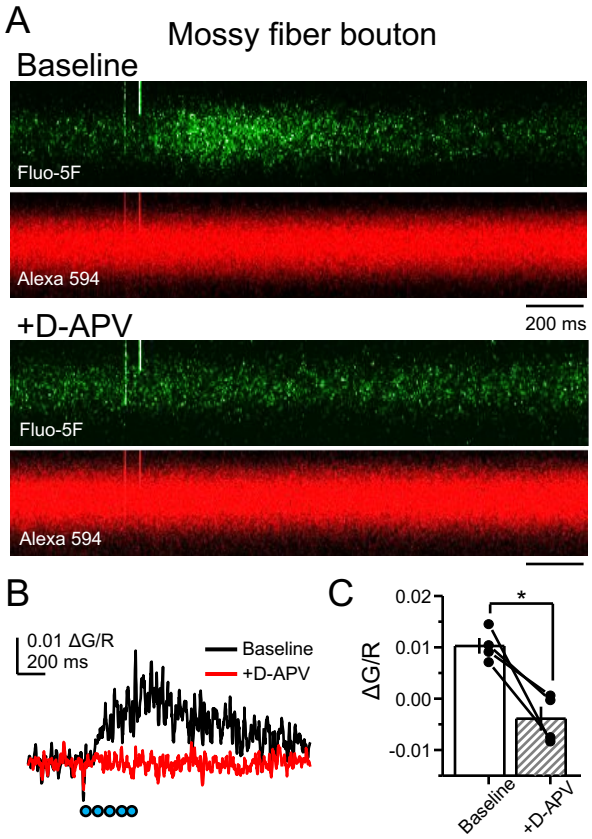

Supplementary Figure 10 related to Figure 6.

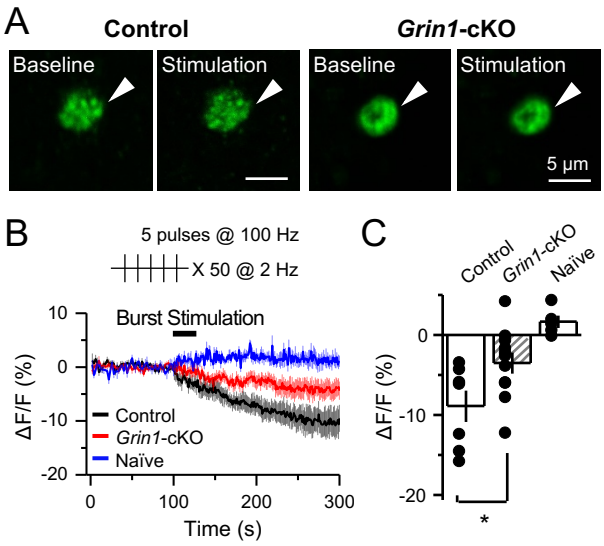

Supplementary Figure 11 related to Figure 7.

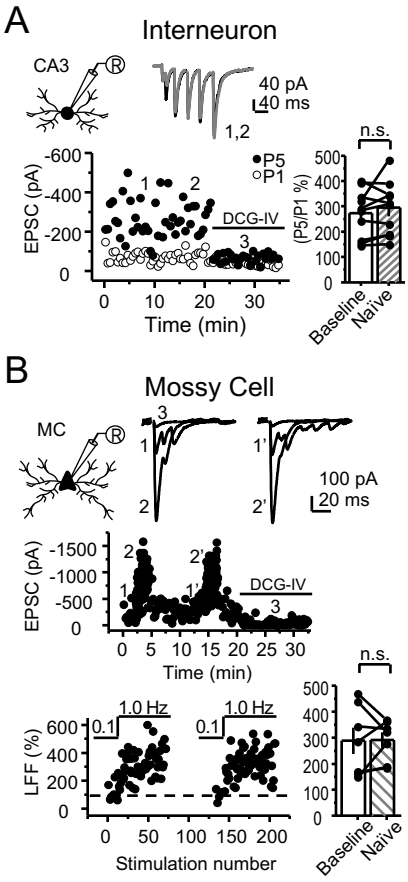

Supplementary Figure 12 related to Figure 8.